

List of Publications

- [1] Saurabh J. Hazarika, D. Mohanta, "Inorganic fullerene-type WS₂ nanoparticles: processing, characterization and its photocatalytic performance on malachite green", *Applied Physics A* (2017) 123:381.
- [2] Saurabh Jyoti Hazarika, Dambarudhar Mohanta, "Exfoliated WS₂ nanosheets: optical, photocatalytic and nitrogen-adsorption/desorption characteristics", *Bulletin of Material Science* (2018) 41:163.
- [3] Saurabh Jyoti Hazarika, Dambarudhar Mohanta, "Excitation dependent light emission and enhanced photocatalytic response of WS₂/C-dot hybrid Nanoscale systems", *Journal of Luminescence* 206 (2019) 530.
- [4] Saurabh Jyoti Hazarika, Dambarudhar Mohanta, "Revealing mechanical, tribological and surface-wettability features of nanoscale inorganic fullerene (IF)-type tungsten disulfide (WS₂) dispersed in a polymer", *Journal of Material Research* (Under review).

List of other Publication


- [1] Saurabh J Hazarika, Dambarudhar Mohanta, "Effect of ion irradiation on nanoscale TiS₂ systems with suppressed Titania phase", *Journal of Physics: Conference Series* 765 (2016) 012007.

List of Conferences

1. Presented poster at National conference 'Condensed Matter Days, 2015 held at Visva-Bharati University, Santiniketan, Kolkata (27th-29th Aug).
2. Presented oral paper at National conference 'Condensed Matter Days, 2016 held at Mizoram University (29th-31st Aug).
3. Presented poster at National conference on soft and hard condensed matter Physics, NCHSCMP-2017 (2nd-4th March) held at Tezpur University.
4. Presented poster at National conference 'Condensed Matter Days, 2017 held at Tezpur University (29th-31st Aug).
5. Presented oral paper at National conference on soft and hard condensed matter Physics, NCHSCMP-2, 4-6 March, 2019 held at Tezpur University.

Addenda

Inorganic fullerene-type WS₂ nanoparticles: processing, characterization and its photocatalytic performance on malachite green

Saurabh Jyoti Hazarika¹ · Dambarudhar Mohanta¹ 

Received: 2 January 2017 / Accepted: 7 April 2017
© Springer-Verlag Berlin Heidelberg 2017

Abstract In this work, we have employed a hydrothermal route for the synthesis of fullerene-type tungsten disulfide (WS₂) nanoparticles. X-ray diffraction analysis signifies a hexagonal crystal structure of WS₂ with the crystallites experiencing preferred orientations along (002) and (103) planes. The agglomerated nanoparticles and inorganic fullerene (IF)-type structures are apparently observable from the high-resolution electron micrographs. Raman spectrum shows prominent E_{2g}^1 and A_{1g} modes emanating from the IF nano-WS₂ system. The Tauc's plot obtained from the optical absorption data predicts a direct band gap of ~ 1.91 eV for the nano-WS₂ system; whereas, photoluminescence analysis reveals a broad emission peak located at ~ 638 nm and is ascribed to the associated transition from the indirect to direct nature of the band gap. The photocatalytic decomposition of malachite green (MG) solution (30 mg/l) by WS₂ (100 mg/l) under UV and visible light irradiation has been evaluated. The latter condition exhibited a better photocatalytic response with the MG degradation as high as 71.2%, revealed for 120 min. Photocatalytic and optoelectronic features of IF-type nano-WS₂ would bring new insights not only to resolve issues related to environmental hazards, but also in functional devices of technological relevance.

1 Introduction

The pioneering works on atomically thin graphene layers have paved the way for the investigation of 2D layered materials in recent years [1]. The recent research works in the field of graphene has shown some extraordinarily interesting properties including its applicability in the field of bioelectronics for artificial dynamic synapse [2]. Undoubtedly, graphene offers a unique platform in the sense that, with the use of electrical gating Fermi level can be easily tuned along with the band gap opening. The gate-controlled graphene electrode-based random access memory with an adaptable single-electron transistor window has been worked out [3]. Due to the lack of inherent band gap, the electronic components made from graphene cannot be switched on and off in an efficient manner, which gives a low turn on and off time ratios [4]. To overcome this technical limitation, there is an urgent need to exploit other 2D layered materials, known as transition metal dichalcogenide (TMDC) systems. TMDCs have generalized formula MX₂, where M is a transition metal element (group IV or V), and X is a chalcogen [5]. In several applications, these materials are advantageous over graphene as they possess sizable band gap, better exfoliation and handling capability, low phonon energy, etc. These materials, in conjunction with other 2D materials, are capable of making high-performance optoelectronic components over a broad spectral range [3, 6]. On the other hand, monochalcogenides of group IV elements (like Ge and Si), which possess black phosphorus-type structure along with other low symmetry TMDC, such as rhenium disulphide (ReS₂) and rhenium diselenide (ReSe₂) exhibit unique physical properties for numerous applications in the field of nano-electronics, nanophotonics, piezoelectric devices and thermo-electronics [7].

✉ Dambarudhar Mohanta
best@tezu.ernet.in

¹ Nanoscience and Soft Matter Laboratory, Department of Physics, Tezpur University, Napaam, Tezpur, Assam 784 028, India

In the past decade, molybdenum disulfide (MoS_2), which is an important member of the family of TMDCs, has received widespread interest among the researchers. MoS_2 has been extensively studied compared to tungsten disulphide (WS_2) counterpart [8–10]. However, WS_2 has not been evaluated in great detail due to insufficient information as regards its physical properties and processibility conditions. WS_2 has drawn research interest owing to exhibition of its matchless value in the field of hydrogen storage, micro-electrode material, solid lubrication, catalysis, etc. [11–13]. The crystal structure of WS_2 consists of an S–W–S single-layer bonded Van der Waals force. WS_2 can adopt a single graphite-like structure, or quantum dot nanoparticles, thus triggering the urge among the physicists to study this system [8]. WS_2 is a semiconductor with a band gap of 1.35 eV, thus expanding the light absorption region to infrared (IR) region, i.e. 910 nm [8]. The band gap of WS_2 can also be controlled from indirect to direct type by exfoliating the bulk WS_2 to nanosheets [14]. Nanoscale WS_2 has also demonstrated its potential use in advanced applications, such as photothermal therapy for destroying cancer cells by converting the absorbed near IR light into heat [8]. As a common, yet important application of WS_2 , its use as a nano-photocatalyst is tremendous. In this regard, a few reports have highlighted photocatalytic studies of pure and WO_3 -coupled WS_2 systems [15, 16]. Under UV illumination for 10 min, the mesoporous WS_2 nanosheets were shown to degrade rhodamine B (RhB) up to 21% [15]. In contrast, much enhanced photocatalytic degradation of phenol has been witnessed upon extended UV illumination of polycrystalline mixed WO_3/WS_2 systems [16].

The present work highlights hydrothermal synthesis of inorganic fullerene (IF)-type WS_2 nanoparticles and their photocatalytic responses considering both visible and UV exposure and with malachite green (MG) as the target agent. Structural, morphological, optical and Raman analyses have also been discussed.

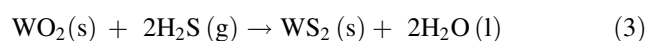
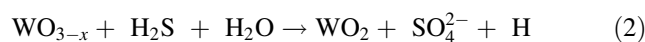
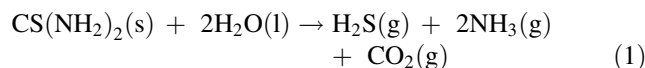
2 Experimental: materials and methods

2.1 Synthesis of inorganic fullerene-type nano- WS_2 system

We have attempted a two-step hydrothermal process for the production of nano- WS_2 . The chemicals used in the synthesis were of analytical grade and have been used without further purification. While sodium tungstate ($\text{Na}_2\text{WO}_4 \cdot 2\text{H}_2\text{O}$) (Rankem, 98% pure) has been considered as the source of tungsten, thiourea ($\text{CH}_4\text{N}_2\text{S}$) (Merck, 99% pure) was used as the source of sulfur. First, 1.64 g of sodium tungstate, 0.69 g of hydroxylamine hydrochloride ($\text{NH}_2 \cdot \text{OH} \cdot \text{HCl}$) (Merck, 98% pure) and 1.52 g of thiourea are

dissolved in 30 ml of deionized Millipore® water. The mixture was kept under constant stirring for 25 min, with the pH value adjusted to 6 by adding few drops of ammonia water. The solution is transferred to a 50-ml teflon-lined stainless steel autoclave, which was properly sealed and then subjected to oven heating at a temperature of 180 °C, for 24 h. The collected product is washed several times with distilled water and then with ethanol under centrifugation (3500 rpm) for about 15 min. The precipitate obtained is oven dried at a temperature of 60 °C, for 10 h. The resultant product that appeared to be blonde yellow in color is labeled as S_1 . The light colored powder obtained resembles that of an intermediate product (WO_{3-x}) in the formation of WS_2 which may arise due to the inadequacy of sulphur in the reaction process [17].

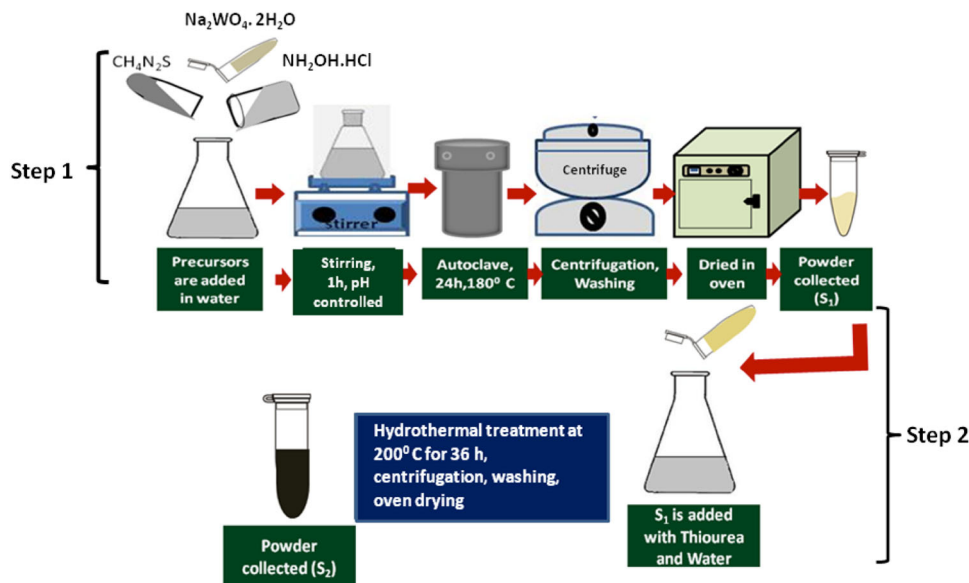
In the second step, 0.58 g of S_1 (obtained through the first step) is mixed with 0.78 g of thiourea and 40 ml deionized water in a conical flask and subjected to vigorous stirring for 20 min. Then, the solution is poured in a 50-ml Teflon-lined stainless steel autoclave, sealed airtight and kept in an oven maintained at a temperature of 200 °C, for 36 h. The product is centrifuged (3500 rpm, 5 min), washed with distilled water and finally, cleansed with ethanol suitably. The product is then dried in an oven (80 °C) for about 10 h. The steps as regards formation of the final nano- WS_2 product (S_2) is illustrated in Fig. 1. The chemical equations involved are as given below [17]:



2.2 Characterization techniques employed

To exploit the structural and crystallographic properties, X-ray diffraction (XRD) technique was employed using a MiniFlex Rigaku X-ray diffractometer equipped with a CuK_α source ($\lambda = 1.543 \text{ \AA}$). The morphological details of the as-synthesized WS_2 samples were revealed through scanning electron microscopy (JEOL, 6390LV) and transmission electron microscopy (FEI, Tecnai) imaging studies. The elemental composition of the samples was confirmed from the EDX spectra. On the other hand, luminescence characteristics and phonon-assisted vibrational modes are exploited through the luminescence spectrophotometer (Hitachi 2700 FL) and Raman spectrometer (Renishaw, Wotton-under-Edge); respectively. The optical absorption responses as obtained through UV–Vis spectroscopy (UV 2450, Shimadzu Corporation) are used for estimating energy band gap as well as photocatalytic degradation efficiency.

Fig. 1 Schematic diagram of the sequential steps involved in processing IF nano-WS₂ system



2.3 Execution of photocatalytic experiment

To analyze the photocatalytic efficiency of the as-prepared nano-WS₂ samples, we have chosen malachite green (MG) as the target to be decomposed. MG is an organic compound that is used as a dyestuff and controversially as an antimicrobial in aquaculture [18]. All around the globe, researchers are trying hard to find suitable ways to degrade harmful organic dyes and pollutants. The photoactivity of the nano-WS₂ samples has been investigated both under UV and day light illumination conditions. To perform the experiment, 100 mg/L of the WS₂ nanoparticles is first added to 30 mg/L of the MG, and then subjected to stirring for about 1 h in dark. In the next step, the mixture is ultrasonicated for about half an hour. The collected sol is then placed inside a cabinet which has the provision for UV lamp as well as the incandescent lamp, the latter being used as the source of visible light. The samples are placed on the base of the chamber at a distance of 12 cm from the UV source ($\lambda = 365$ nm) and the polychromatic visible light source used independently. The WS₂ nanocatalyst-loaded dye was irradiated for 15, 30, 45, 60 and 120 min. Next, 5 ml of the MG solution is taken for optical absorption analysis, knowing that the peak maxima for the initial absorption of MG appears at ~ 617 nm [19]. The percentage of decomposition of the MG under UV and visible light irradiation for various durations of UV exposure is given by:

$$\% \text{ degradation} = \left(\frac{C_0 - C_t}{C_0} \right) \times 100 \quad (4)$$

where, C_0 and C_t represent concentration of the MG solution before and after irradiation.

3 Results and discussion

3.1 Structural and morphological analyses

The XRD patterns of the as-prepared samples are shown in Fig. 2a, b. It can be seen that the sample S_1 exhibits diffraction peaks which is similar to that of $WO_3 \cdot 5H_2O$ (JCPDS File No. 44-0363) and $WO_3 \cdot 33H_2O$ (JCPDS File No. 35-1001) [17]. Attributed to (002) plane of hexagonal WS₂, the diffraction peak at $2\theta \sim 15.20^\circ$ in sample S_1 is marginally shifted to 14.32° in system S_2 (JCPDS File No. 08-0237) [17]. The other peaks at 28.76° , 33.42° , 39.57° , 44.28° , 49.65° and 58.53° corresponded to (004), (101), (103), (006), (105) and (110) planes of the hexagonal WS₂, respectively. The sharp peaks corresponding to the (002) and (103) planes suggest competitive growth of the crystallites along these directions. The sharp diffraction lines are also shown in the figure in accordance with respective JCPDS files. From the analyses of diffractograms, it is quite apparent that the synthesized product obtained through the additional step ensured the desired phase of the nano-WS₂ system. The average crystallite size (D) of the WS₂ nanoparticles was calculated using the Williamson–Hall (W-H) plot by choosing the most prominent diffraction peaks, such as (004), (101), (103), (006), (105) and (110). The W-H expression is given by:

$$\beta \cos \theta = 4\epsilon \sin \theta + 0.9 \lambda / D, \quad (5)$$

where λ is the wavelength of the X-ray radiation ($\lambda = 0.1543$ nm for CuK_α line), 2θ is the diffraction angle, β is the line width at half maximum height and ϵ is the mean lattice strain. As found in Fig. 2b, by plotting $\beta \cos \theta$ vs. $4 \sin \theta$, the size component can be obtained directly from the intercept of the straight line on the y-axis [20].

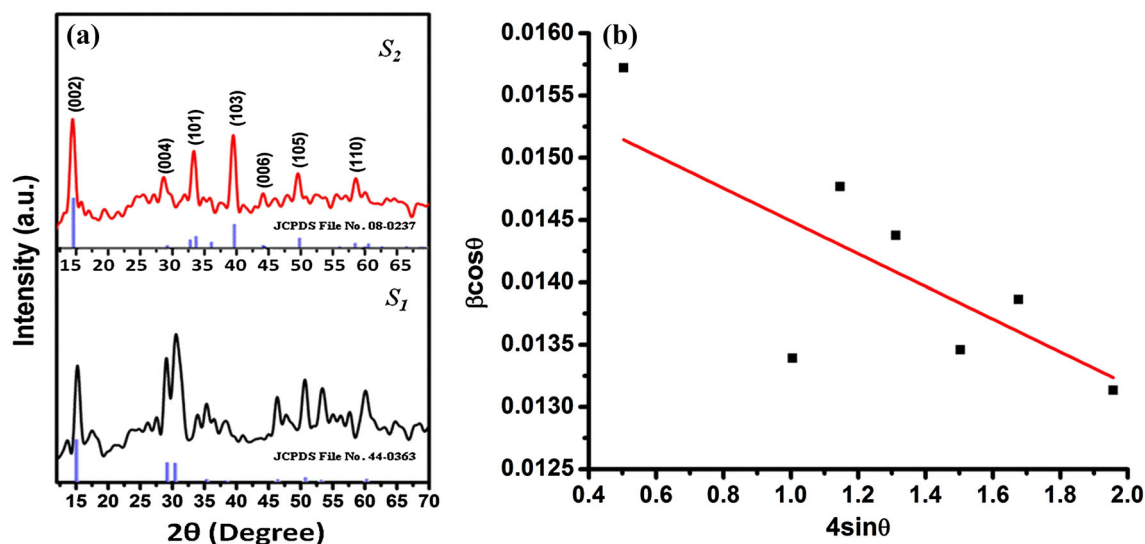


Fig. 2 **a** X-ray diffractograms of the prepared samples and **b** the W-H plot for sample S_2

Similarly, microstrain ε can be evaluated from the desired slope. Using the W-H formula, the average crystallite size was calculated to be ~ 7.7 nm and the microstrain as, -1.3×10^3 . The negative strain corresponds to relaxed nature of the crystallites, whereas positive strain indicates compaction of the crystallites [21]. Using conditions relevant to hexagonal structure, the crystal lattice parameters can be found as, $a = b = 3.16$ Å and $c = 12.28$ Å.

The EDX spectra of the two samples S_1 and S_2 are shown in Fig. 3. The presence of elements W, O and S is evident from the EDX spectrum of S_1 . However, the amount of sulphur present in S_1 is quite small. The amount of sulphur present is significantly high in sample S_2 , as compared to S_1 . Since no oxygen peak is witnessed in the EDX spectrum of sample S_2 , it substantiates the development of high-yield WS_2 phase, free from oxide content. Moreover, the sample S_2 gave the atomic ratio of W to S as, 1:1.83. Since the formation of phase-pure WS_2 is ascertained, further characterization wrt imaging was considered for the sample S_2 .

Figure 4A shows the SEM micrographs of the desired WS_2 nanosystem. Here, we could clearly notice formation of clustered nanoparticles similar to an earlier work [22]. In fact, the structural morphology of the WS_2 nanostructures largely depends on the reaction time and processing temperature [23]. The agglomeration of particles is caused due to the multi-nuclei attachment, which serves as the possible mechanism of growth along (002) direction [24]. The low and high magnification micrographs are shown in Fig. 4A(a), A(b), respectively. Figure 4B(a–d) depicts the TEM imaging feature of the nano- WS_2 system. Apparently, the TEM image reveals development of fullerene-shaped structures of nano- WS_2 system [Fig. 4B(a), (c)]. The size distribution is shown in the inset of Fig. 4B(a). The

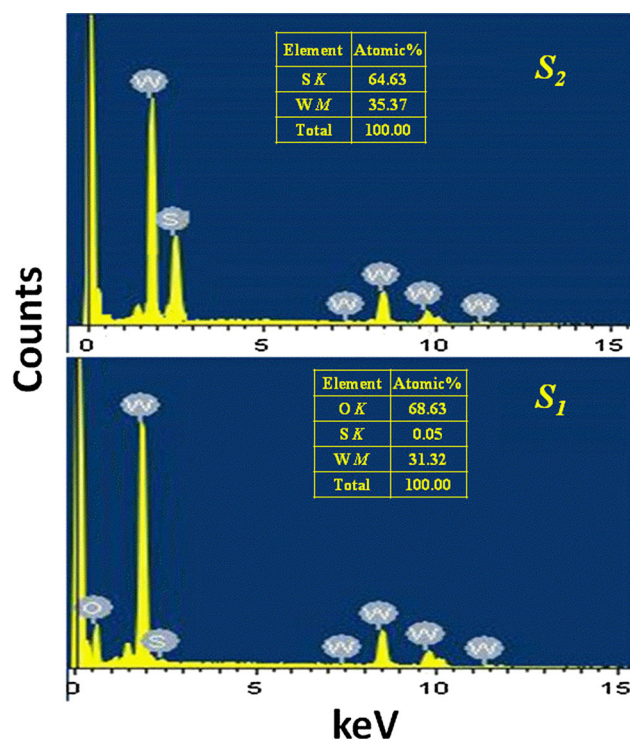
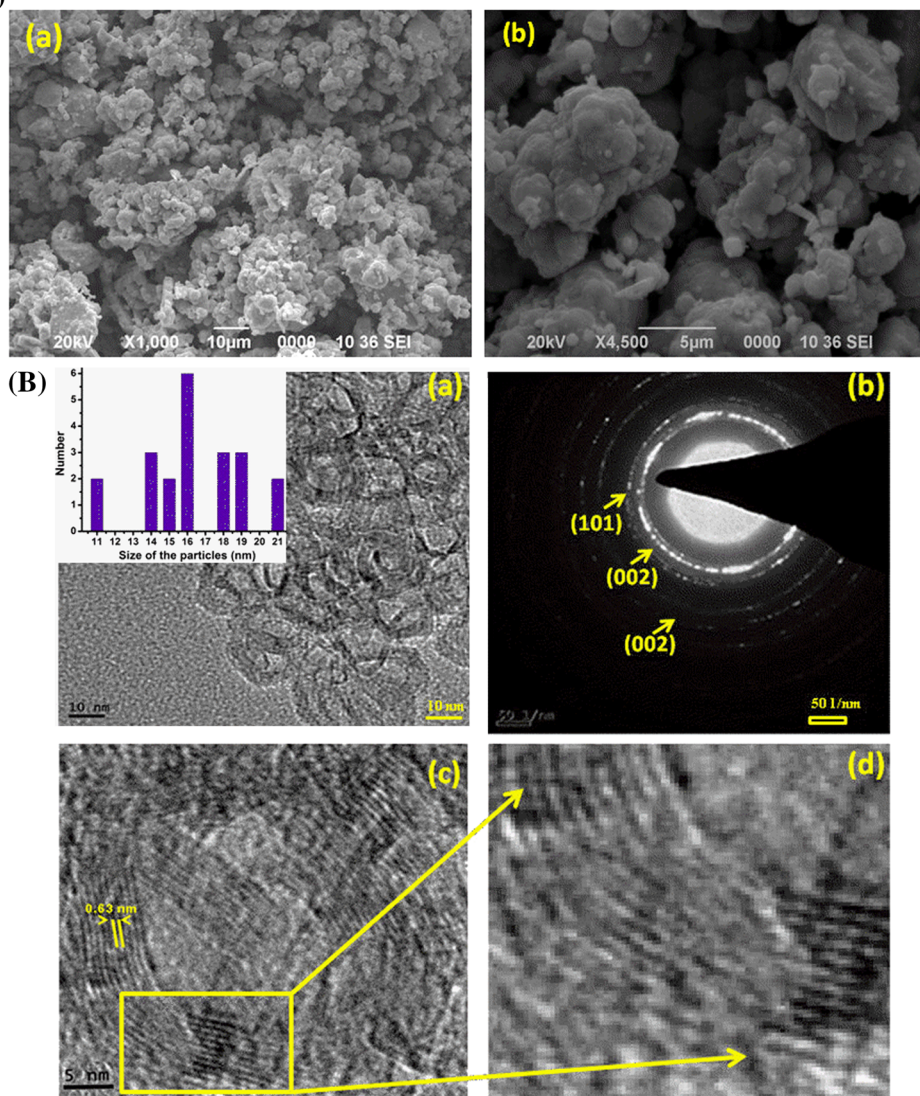


Fig. 3 EDX spectra of the as-prepared nano- WS_2 samples

formation of diffused rings as witnessed in the SAED micrograph [Fig. 4B(b)] suggests the polycrystalline nature of the synthesized product which could arise due to the presence of surface defects on nano- WS_2 system [25]. The hollow core IF fullerene-type structures with bent lattice edges can be found in Fig. 4B(c). In the magnified image of the corner of an individual IF structure we noticed that a corner is essentially formed from a series of bent lattice planes [Fig. 4B(d)]. In this regard, strain relief mechanism

Fig. 4 **A** SEM micrographs of the as-prepared nano-WS₂ system: **a** low magnification, **b** high magnification. **B** **a** TEM micrograph depicting distributed view of IF-type WS₂ nanoparticles with a histogram on size distribution (*inset*), **b** SAED pattern, **c** a single IF nano-WS₂ structure and **d** enlarged view of a segment showing the bent lattice structure of the WS₂ nanosystem



has been proposed for exhibition of such unusual morphology/structures [26]. The average outer diameter of the IF nano-WS₂ particles is estimated to be ~ 16 nm, with an interlayer spacing of 0.63 nm.

3.2 Vibrational analysis using Raman and FTIR spectroscopy techniques

Figure 5a represents the Raman spectrum of the synthesized nano-WS₂ system measured with an excitation wavelength, $\lambda_{\text{ex}} \sim 514$ nm. Raman spectroscopy is a non-invasive, yet important tool to reveal structural information as regards number of layers, defects, doping levels, strain effects and other factors. In fact, bulk WS₂ shows two major bands corresponding to E_{2g}^1 and A_{1g} modes essentially located at ~ 351 and 420 cm^{-1} , respectively [27]. In our case, the two vibronic bands are witnessed at ~ 352.4

and 419.5 cm^{-1} which correspond to the first-order modes at the Brillouin zone; with first being an in-plane mode E_{2g}^1 and second identified as out-of-plane mode A_{1g} [28]. These values are slightly different when compared to those of the bulk WS₂ crystal. The slight shift of A_{1g} mode towards higher wavelength side may be due to the decrease in interlayer Van der Waals interaction which causes weaker restoring forces in the vibration as we move from bulk to few layers of WS₂ [14]. On the other hand, the blue shift in E_{2g}^1 is attributed to the reduced long-range Coulomb interaction between the effective charges caused by an increase in the dielectric screening on stacking-induced changes in the interlayer bonding [14]. The ratio of intensities of the E_{2g}^1 and A_{1g} calculated stands at 0.61 which is higher than that of bulk WS₂ but lower than the mono, bi and tri-layered WS₂ nanosystems [29]. Thus our

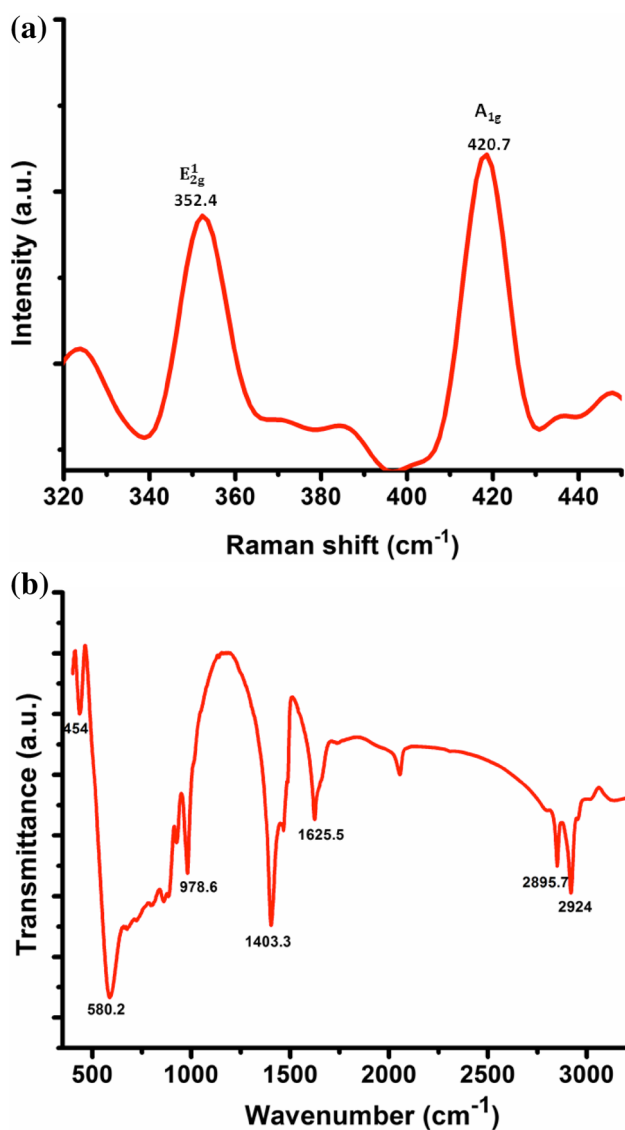


Fig. 5 **a** Raman spectrum and **b** FTIR spectrum of the as-prepared IF-type WS₂ nanosystem (sample S₂)

IF-type nano-WS₂ must comprise sufficient number of layers which results in a dominant out-of-plane vibration over the in-plane one.

The FTIR spectroscopy essentially offers information regarding the nature of chemical bonding and the molecular structure of the system under study. Figure 5b depicts the FTIR spectrum of the synthesized nano-WS₂ system in the wavenumber range 400–3200 cm⁻¹. A distinct band at 454 cm⁻¹ refers to the characteristic S–S bond of the elemental sulphur [30]. The bands positioned at ~580.2 and 978.6 cm⁻¹ are ascribed to the W–S bond and S–S bond, respectively [31]. The bands found at ~1403.3 and 1625.5 cm⁻¹ are ascribed to the stretching vibrations of the hydroxyl group [31]. Moreover, the vibrational bands at

2895.7 and 2924 cm⁻¹ can be attributed to the atmospheric OH and that is available in the WS₂ system [31].

3.3 Optical band gap calculation and luminescence response

The UV–Vis optical absorption spectrum of the sample S₂ is shown in Fig. 6a. It depicts presence of two weak absorption bands located at ~537 and ~649 nm. Even though these two bands represent characteristic absorption response of IF-WS₂ nanostructures [32, 33], particularly the peak at ~649 nm corresponds to *d*–*d* type transitions of the WS₂ at the center of the Brillouin zone [34]. To determine the band gap of the prepared WS₂ nanoparticles, we have plotted the Tauc's plot using the relation [31], $\alpha h\nu = (h\nu - E_g)^n$, where *h* is the Planck's constant, *v* is the

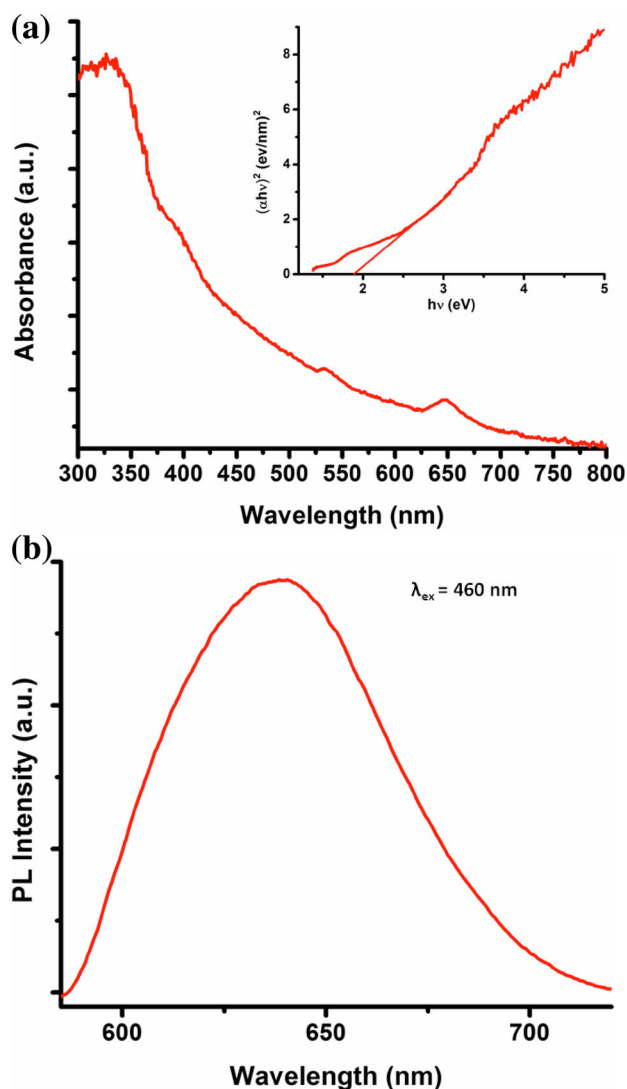


Fig. 6 **a** UV–Vis optical absorption spectrum along with the Tauc's plot (*inset*), and **b** PL spectrum of the IF nano-WS₂ system

frequency of the incident light and α is the absorption coefficient. Putting $n = \frac{1}{2}$ for the direct allowed transitions, the band gap of the prepared WS₂ nanosystem is estimated to be 1.91 eV, which is in good agreement with an earlier report [8].

PL is a versatile tool to exploit the radiative emission and defect-mediated transitions. PL spectroscopy study is necessary to understand the carrier recombination processes to be understood for photocatalysis in latter studies. Figure 6b shows the PL spectrum of the synthesized WS₂ nanosystem acquired under an excitation wavelength of $\lambda_{\text{exc}} = 460$ nm. The broad peak at ~ 638 nm is the outcome of transition from the indirect band gap type to the direct band gap one when the bulk system is thinned down to a few nanometric layers [14]. This peak suggests the separation efficiency of the electron-hole pairs, with superior characteristics due to the presence of surface area and active edges [19]. Reports suggest that a direct gap exists at the *K* points of the Brillouin zone between the spin-orbit split valence band and the doubly degenerate conduction band. The indirect band gap is known to form between a local conduction band which is minimum at the midpoint between *Γ* and *K* and the valence band is maximum at the *Γ* point [14]. The existence of the direct transition can be explained from excitonic radiative relaxation and accordingly, the appearance of PL peak has been observed at energies slightly lower than the 2.05 eV direct band gap of WS₂ [14]. The luminescence pattern is observed to be asymmetrically broadened and with a full-width half-maxima (FWHM) of approximately 183 meV. A broad emission peak suggests that, the transition from indirect to direct nature of the gap is not discrete, but continuous over an inseparable energy band.

3.4 Evaluation of photocatalytic performance of fullerene-type nano-WS₂ system

To investigate photoactivity of the IF WS₂ nanoparticles, we have chosen MG as the target agent under UV and visible light illumination conditions. The UV-Vis absorption response of the organic dye and nano-WS₂ catalyst-loaded MG can be found in Fig. 7a. The WS₂-loaded dye showed a steady fall in the absorbance with increasing the UV exposure time, exhibiting a minimal strength at ~ 617 nm. Conversely, the samples irradiated under visible light showed a rapid drop in the absorbance response as compared to the samples subjected to UV light (Fig. 7a, b). The IF WS₂ nanoparticles tend to exhibit better catalytic efficiency under visible light because of the narrow band gap, which acts as a driving force to activate the redox reaction necessary for the production of hydroxyl radicals [8]. Also, it has been reported that irregular hexagonal-type structures with

ample surface defects served the purpose of a good nanocatalyst under visible light illumination [35]. Also, IF-type particles can have enhanced photocatalytic responses because of the strong optical absorption, large surface area, and documented chemical inertness under illumination [36].

The schematic diagram as regards the mechanism of the photocatalytic activity of the synthesized WS₂ nanosystem is shown in Fig. 8. The host WS₂ nanocatalyst, upon light irradiation would release electrons and holes. The excited electrons are likely to move to the conduction band creating adequate holes in the valence band. These generated charge carriers are likely to be trapped in the active W⁴⁺ and S²⁻ defect sites lest they might recombine with the counterparts to dissipate energy. These carriers would migrate to the nanocatalyst surfaces, resulting in the formation of reactive intermediates. The photoinduced holes and the reactive hydroxyl radicals are profoundly responsible for initiating the redox reaction required for decomposition of the harmful dye/organic pollutant. The hydroxyl radical is produced either by decomposition of water or by a hole reacting with the OH⁻. Since the target MG is in aqueous form; therefore, the water molecule is believed to come in contact with the surface of the nanocatalyst. The OH group or O²⁻ is likely to be trapped by the active sites of the nanocatalyst [37]. The oxygen vacancy centers are easily de-trapped and the electrons are transferred to the adsorbed oxygen which produces the superoxide radicals [38]. Water and hydroxyl ions are transformed to the hydroxyl radicals by the photo-generated holes [39]. These superoxide and hydroxyl radicals being very strong oxidizing agents could easily degrade the complete dye to its constituent products [40]. We observed an increasing trend of degradation of the MG on increasing the irradiation time. As high as 45% decomposition has been witnessed on irradiating the catalyst-loaded dye under UV light for 120 min (Fig. 7c). Conversely, the IF-WS₂ nanocatalyst gives a superbly enhanced decomposition of MG ($\sim 71.2\%$) when subjected to visible light irradiation for 120 min (Fig. 7c). For the sake of comparison, the photocatalytic responses of different MoS₂ and WS₂ nanosystems are presented in Table 1. To name a few, WS₂ nanosheets possess excellent photocatalytic activity over the complete spectrum, from UV to NIR [8]. Also, mesoporous WS₂ nanosheets are shown to be highly stable and efficient even after four cycles of RhB degradation [15]. In case of degradation of phenol by WO₃/WS₂ polycrystalline powders, the photoactivity is highly dependent on the molar ratio of the systems used [16]. Similarly, WS₂/TiO₂ has also shown an improved photocatalytic activity on harmful organic dyes, such as, target MO [41]. In this

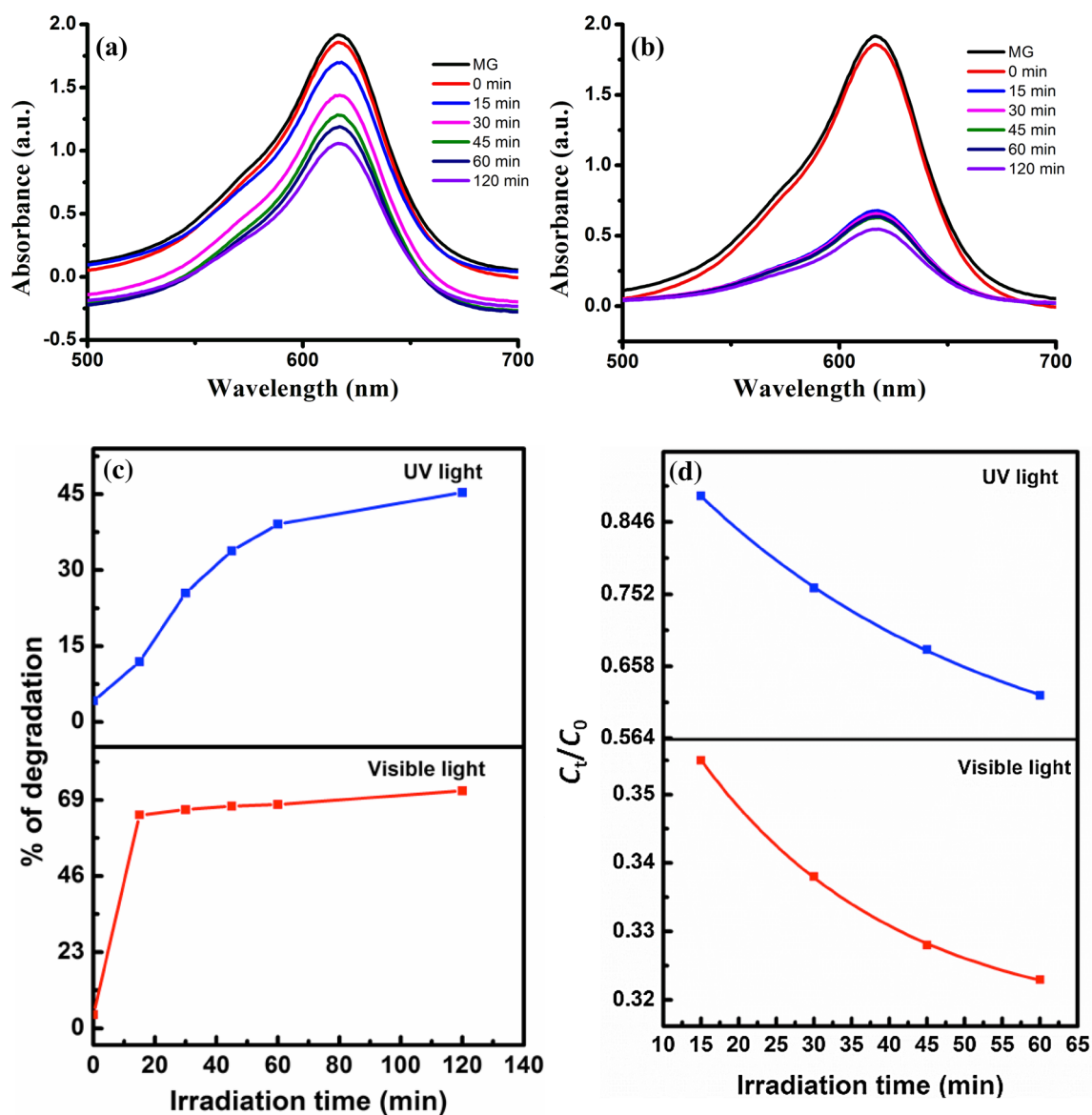


Fig. 7 UV–Vis absorption spectra of MG and IF nano-WS₂ catalyst-loaded dye with different irradiation times: **a** UV illumination, **b** visible light illumination. The percentage of degradation and pseudo-first-order plots under aforesaid conditions are shown in **c**, **d** on a comparative basis

regard, IF-type WS₂ systems, which are rarely discussed in the literature, find its importance in the list of nanocatalysts. The performance of IF-type WS₂ nanosystem on the degradation of MG dye is evaluated through simple kinetics, as discussed below.

The kinetics of photocatalytic degradation of MG at the nanocatalyst surface can be understood through Langmuir–Hinshelwood (L-H) model [42]. For a dilute solution (mM) ($C \ll 1$), it can be expressed in the form of a first-order reaction given by [42]:

$$C_t = C_0 e^{-k_a t} \quad (6)$$

Here, C_0 is the initial concentration of the MG solution, t is the irradiation time and k_a is the pseudo-first-

order rate constant. At $t = t_0$, $C = C_0$, the initial concentration of the target before irradiation. The percentage degradation of MG is represented in Fig. 7c. The plots of C_t/C_0 versus t , for UV and visible light conditions are shown in Fig. 7d. The plots essentially help to predict the pseudo-first-order rate constant, k_a . The rate constants, as obtained directly from the graphs (Fig. 7d), are calculated to be 0.0239 and 0.0414 min⁻¹ for IF nano-WS₂ samples exposed to UV light and visible light, respectively. A higher rate constant for the latter case, suggests that our IF nano-WS₂ are capable of displaying improved photoactivity under visible light illumination than that of UV exposure.

Fig. 8 Schematic of the photocatalytic mechanism expected in the IF nano-WS₂ system

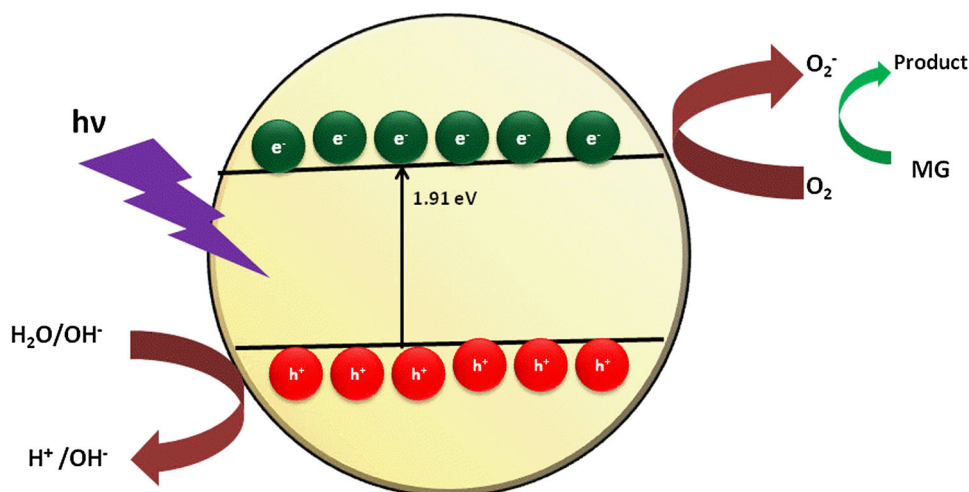


Table 1 A comparative view as regards photocatalytic performance of different nanophotocatalysts (RhB: rhodamine B, MO: methyl orange, CR: congo red, MG: malachite green)

Sl. no.	Material	Illumination source	Target	Degradation time and amount	References
1	SnO ₂ /MoS ₂ nanocomposite	UV light	RhB	50 min (100%)	[9]
2	TiO ₂ /MoS ₂ @ zeolite	Visible light	MO	60 min (95%)	[10]
3	WS ₂ nanosheets	UV light	MO	100 min (100%)	[8]
4	WS ₂ nanosheets	Visible light	MO	300 min (90%)	[8]
5	Mesoporous WS ₂ nanosheets	UV light	RhB	10 min (21%)	[15]
6	WO ₃ /WS ₂ polycrystalline powder	UV light	Phenol	480 min (80%)	[16]
7	WS ₂ /C-dot hybrid nanosheets	Visible light	CR	10 min (12%)	[28]
8	WS ₂ /TiO ₂ nanosystem	Visible light	MO	60 min (95%)	[41]
9	IF-WS ₂ nanosystem	UV light	MG	120 min (45%)	This work
10	IF-WS ₂ nanosystem	Visible light	MG	120 min (71.2%)	This work

4 Conclusion

We have demonstrated a user friendly synthesis and photocatalytic activity of IF-type WS₂ nanoparticles. The hexagonal crystal structure of WS₂ is evident from XRD analysis. The presence of elements W and S has been confirmed from the EDX spectra. The direct band gap of the nano-WS₂, as predicted from the Tauc's plot, is ~1.91 eV. The single distinct peak at 630 nm corresponds to the transition of the band structures from the indirect to direct band gap type. On the other hand, Raman spectrum reveals the presence of one in-plane E_{2g}^1 mode and one A_{1g} out-of-plane mode. The formation of IF-type nanoparticles with an average outer diameter of 16 nm has been observed through the electron micrographs. The photocatalytic efficiency of the synthesized IF WS₂ nanocatalyst under visible light illumination gave a maximum degradation of 71.2% as compared to 45% when illuminated by UV light. Photoactivity studies of TMDCs with inclusion of suitable dopants and radiation effects are in progress.

Acknowledgements The authors acknowledge IUAC, New Delhi (Project: UFR-56322/2014). The authors thank peers and colleagues for their valuable suggestions.

References

1. K.S. Novoselov, A.K. Geim, S.V. Morozov, D. Jiang, Y. Zhang, S.V. Dubonos, I.V. Grigorieva, A.A. Firsov, Electric field effect in atomically thin carbon films. *Science* **306**, 666–669 (2004)
2. H. Tian, W. Mi, X.-F. Wang, H. Zhao, Q.-Y. Xie, C. Li, Y.-X. Li, Y. Yang, T.-L. Ren, Graphene dynamic synapse with modulatable plasticity. *Nano Lett.* **15**, 8013–8019 (2015)
3. H. Tian, H. Zhao, X.F. Wang, Q.Y. Xie, H.Y. Chen, M.A. Mohammad, C. Li, W.T. Mi, Z. Bie, C.H. Yeh, Y. Yang, H.S. Philip Wong, P.W. Chiu, T.L. Ren, In situ tuning of switching window in a gate-controlled bilayer graphene-electrode resistive memory device. *Adv. Mater.* **27**, 7767–7774 (2015)
4. Q.H. Wang, K.K. Zadeh, A. Kis, J.N. Coleman, M.S. Strano, Electronics and optoelectronics of two-dimensional transition metal dichalcogenides. *Nat Nanotechnol* **7**, 699–712 (2012)
5. S. Bhattacharyya, A.K. Singh, Semiconductor-metal transition in semiconducting bilayer sheets of transition-metal dichalcogenides. *Phys. Rev. B.* **86**, 075454 (2012)

6. H. Tian, M.L. Chin, S. Najmaei, Q. Guo, F. Xia, H. Wang, M. Dubey, Optoelectronic devices based on two-dimensional transition metal dichalcogenides. *Nano Res.* **9**, 1543–1560 (2016)
7. H. Tian, J. Tice, R. Fei, V. Tran, X. Yan, L. Yang, H. Wang, Low-symmetry two-dimensional materials for electronic and photonic applications. *Nano Today* **11**, 763–777 (2016)
8. Y. Sang, Z. Zhao, M. Zhao, P. Hao, Y. Leng, H. Liu, From UV to near-infrared, WS₂ nanosheet: a novel photocatalyst for full solar light spectrum photodegradation. *Adv. Mater.* **27**, 363–369 (2015)
9. S.V.P. Vattikuti, C. Byon, C.V. Reddy, R.V.S.S.N. Ravikumar, Improved photocatalytic activity of MoS₂ nanosheets decorated with SnO₂ nanoparticles. *RSC Adv.* **5**, 86675–86684 (2015)
10. W. Zhang, X. Xiao, L. Zheng, C. Wan, Fabrication of TiO₂/MoS₂@zeolite photocatalyst and its photocatalytic activity for degradation of methyl orange under visible light. *Appl. Surf. Sci.* **358**, 468–478 (2015)
11. D. Voiry, H. Yamaguchi, J. Li, R. Silva, D.C.B. Alves, T. Fujita, M.W. Chen, T. Asefa, V.B. Shenoy, G. Eda, M. Chhowalla, Enhanced catalytic activity in strained chemically exfoliated WS₂ nanosheets for hydrogen evolution. *Nat. Mater.* **12**, 850 (2013)
12. L. Rapoport, Y. Bilik, Y. Feldman, M. Homyonfer, S.R. Cohen, R. Tenne, Hollow nanoparticles of WS₂ as potential solid-state lubricants. *Nature* **387**, 791–793 (1997)
13. R. Levi, O. Bitton, G. Leitus, R. Tenne, E. Joselevich, Field-effect transistors based on WS₂ nanotubes with high current-carrying capacity. *Nano Lett.* **13**, 3736–3741 (2013)
14. H.R. Gutiérrez, N. Perea-Lopez, A.L. Elias, A. Berkdemir, B. Wang, R. Lv, F. Lopez-Urias, V.H. Crespi, H. Terrones, M. Terrones, Extraordinary room-temperature photoluminescence in triangular WS₂ monolayers. *Nano Lett.* **13**, 3447–3454 (2013)
15. S.V.P. Vattikuti, C. Byon, C.V. Reddy, Preparation and improved photocatalytic activity of mesoporous WS₂ using combined hydrothermal-evaporation induced self-assembly method. *Mater. Res. Bull.* **75**, 193–203 (2016)
16. A. Di Paola, L. Palmisano, V. Augugliaro, Photocatalytic behavior of mixed WO₃/WS₂ powders. *Catal. Today* **58**, 141–149 (2000)
17. Y. Shang, J. Xia, Z. Xu, W. Chen, Hydrothermal synthesis and characterization of quasi 1D tungsten disulfide nanocrystal. *J. Disp. Sci. Technol.* **26**, 635–639 (2005)
18. S. Srivastava, R. Sinha, D. Roy, Toxicological effects of malachite green. *Aquat. Toxicol.* **66**, 319–329 (2004)
19. G. Parshetti, S. Kalme, G. Saratale, S. Govindwar, Biodegradation of Malachite Green by *Kocuria rosea* MTCC 1532. *Acta Chim. Slov.* **53**, 492–498 (2006)
20. S.W. Park, J.T. Jang, J. Cheon, H.H. Lee, D.R. Lee, Y. Lee, Shape dependent compressibility of TiO₂ anatase nanoparticles. *J. Phys. Chem. C* **112**(26), 9627–9631 (2008)
21. S. Hazarika, D. Mohanta, Extraction and characterization of mixed phase KNO₂–KNO₃ nanocrystals derived from flat-leaf green spinach. *Phys. Scr.* **87**, 015603-1–5 (2013)
22. E. García-Lecina, I. García-Urrutia, J.A. Díez, J. Fornell, E. Pellicer, J. Sort, Codeposition of inorganic fullerene-like WS₂ nanoparticles in an electrodeposited nickel matrix under the influence of ultrasonic agitation. *Electrochim. Acta* **114**, 859–867 (2013)
23. S. Cao, T. Liu, S. Hussain, W. Zeng, X. Peng, F. Pan, *Mater. Lett.* **129**, 205–208 (2014)
24. J.L. Elechiguerra, J. Reyes-Gasga, M. Jose-Yacamán, The role of twinning in shape evolution of anisotropic noble metal nanostructure. *J. Mater. Chem.* **16**, 3906–3919 (2006)
25. Yu Zhang, Y. Zhang, Q. Ji, J. Ju, H. Yuan, J. Shi, T. Gao, D. Ma, M. Liu, Y. Chen, X. Song, H.Y. Hwang, Y. Cui, Z. Liu, Controlled growth of high-quality monolayer WS₂ layers on sapphire and imaging its grain boundary. *ACS Nano* **7**, 8963–8971 (2013)
26. C. Schuffenhauer, R. Popovitz-Biro, R. Tenne, Synthesis of NbS₂ nanoparticles with (nested) fullerene-like structure (IF). *J. Mater. Chem.* **12**, 1587–1591 (2002)
27. H. Zeng, G-B. Liu, J. Dai, Y. Yan, B. Zhu, R. He, L. Xie, S. Xu, X. Chen, W. Yao, X. Cui, Optical signature of symmetry variations and spin-valley coupling in atomically thin tungsten dichalcogenides. *Sci. Rep.* **3**, 1608 (2013)
28. P. Atkin, T. Daeneke, Y. Wang, B.J. Carey, K.J. Berean, R.M. Clark, J.Z. Ou, A. Trinchì, I.S. Cole, K. Kalantar-zadeh, 2D WS₂/carbon dot hybrids with enhanced photocatalytic activity. *J. Mater. Chem. A* **4**, 13563–13571 (2016)
29. A. Berkdemir, H.R. Gutiérrez, A.R. Botello-Méndez, N. Perea-López, A.L. Elías, C.I. Chia, B. Wang, V.H. Crespi, F. López-Urías, J.C. Charlier, H. Terrones, M. Terrones, Identification of individual and few layers of WS₂ using Raman spectroscopy. *Sci. Rep.* **3**, 1755 (2013)
30. J. Coates, Interpretation of infrared spectra, a practical approach in encyclopedia of analytical chemistry, ed. R.A. Meyers (Wiley, Chichester, 2000), p. 10829
31. S.V.P. Vattikuti, C. Byon, Effect of CTAB surfactant on textural, structural, and photocatalytic properties of mesoporous WS₂. *Sci. Adv. Mater.* **7**(12), 2639–2645 (2015)
32. Y. Feldman, G.L. Frey, M. Homyonfer, V. Lyakhovitskaya, L. Margulis, H. Cohen, G. Hodes, J.L. Hutchison, R. Tenne, Bulk synthesis of inorganic fullerene-like MS₂ (M = Mo, W) from the respective trioxides and the reaction mechanism. *J. Am. Chem. Soc.* **118**, 5362–5367 (1996)
33. G.L. Frey, S. Elani, M. Homyonfer, Y. Feldman, R. Tenne, Optical-absorption spectra of inorganic fullerene like MS₂ (M=Mo, W). *Phys. Rev. B* **57**, 6666 (1998)
34. S.M. Notley, High yield production of photoluminescent tungsten disulphide nanoparticles. *J. Coll. Interf. Sci.* **396**, 160–164 (2013)
35. S.V.P. Vattikuti, C. Byon, V. Chitturi, Selective hydrothermally synthesis of hexagonal WS₂ platelets and their photocatalytic performance under visible light irradiation. *Superlattices Microstruct.* **94**, 39–50 (2016)
36. H. Tributsch, *Structure and bonding*, vol. 49 (Springer, Berlin, 1982), p. 127
37. N. Paul, A. Deka, D. Mohanta, Augmented photocatalytic activity and luminescence response of Tb³⁺ doped nanoscale titania systems. *J. Appl. Phys.* **116**, 144902-1–7 (2014)
38. S. Bingham, W.A. Daoud, Recent advances in making nano-sized TiO₂ visible-light active through rare-earth metal doping. *J. Mater. Chem.* **21**, 2041–2050 (2011)
39. K.M. Parida, N. Sahu, Visible light induced photocatalytic activity of rare earth titania nanocomposites. *J. Mol. Catal. A* **287**, 151–158 (2008)
40. T. Peng, D. Zhao, H. Song, C. Yan, Preparation of lanthana-doped titania nanoparticles with anatase mesoporous walls and high photocatalytic activity. *J. Mol. Catal. A* **238**, 119–126 (2005)
41. L. Zheng, W. Zhang, X. Xiao, Preparation of titanium dioxide/tungsten disulfide composite photocatalysts with enhanced photocatalytic activity under visible light. *Korean J. Chem. Eng.* **33**, 107–113 (2016)
42. U.I. Gaya, A.H. Abdullah, Heterogeneous photocatalytic degradation of organic contaminants over titanium dioxide: a review of fundamentals, progress and problems. *J. Photochem. Photobiol. C* **9**, 1–12 (2008)



Exfoliated WS₂ nanosheets: optical, photocatalytic and nitrogen-adsorption/desorption characteristics

S J HAZARIKA and D MOHANTA* 

Nanoscience and Soft Matter Laboratory, Department of Physics, Tezpur University, PO: Napaam, Tezpur, Assam 784028, India

*Author for correspondence (best@tezu.ernet.in)

MS received 19 January 2018; accepted 24 March 2018

Abstract. In this work, we report on structural, optical, photocatalytic and nitrogen adsorption–desorption characteristics of WS₂ nanosheets developed *via* a hydrothermal route. X-ray diffraction (XRD) studies have revealed a hexagonal crystal structure, whereas nanodimensional sheets are apparently observed in scanning and transmission electron microscopy (SEM and TEM) micrographs. As compared to the bulk counterpart, the WS₂ nanosheets exhibited a clear blue shift. Through Brunauer–Emmett–Teller (BET) surface area analysis, average surface area, pore volume and pore size of the NSs were calculated as 211.5 m² g⁻¹, 0.433 cc g⁻¹ and 3.8 nm, respectively. The photocatalytic activity of the WS₂ nanosheets was also examined with malachite green (MG) as the target dye under both UV and day light (visible) illumination conditions. Accordingly, a degradation efficiency as high as 67.4 and 86.6% were witnessed for an irradiation time duration of 60 min. The nano-WS₂ systems have immense potential in optoelectronics, solid-lubrication and other next generation elements.

Keywords. Nanosheets; photocatalysis; TMDC; sorption process.

1. Introduction

Owing to their immense potential in the fields of optoelectronics, nanoelectronics and nanophotonics, graphene and other layered systems have captured a great deal of interest amongst material scientists and researchers [1]. Layered materials, especially the transition metal dichalcogenides (TMDCs) have unusually exciting properties when exist in layered form. While possessing the general formula MX₂ (where M = Mo, W, Ta, etc. and X = S, Se, Te, etc.), the systems characterize an indirect band gap in the bulk form, and turns into a direct band gap when exfoliated to a few layers or monolayer [2].

In the family of TMDCs, tungsten disulphide (WS₂) is a technologically important member with matchless power in the fields of optoelectronics, catalysis and lubrication [3]. One of the most remarkable applications of WS₂ is to use it as a photoactive material and as a photocatalyst. Being a narrow band gap semiconductor ($E_g = 1.9$ eV), WS₂ is responsive to both UV and visible light illuminations. This allows the nanoscale WS₂ to act as an advanced photocatalytic agent as compared to the traditional photocatalysts, such as TiO₂, SnO₂ and ZnO, which are generally efficient only under UV light irradiation [4]. One of the essential features of a good photocatalyst is large surface-to-volume ratio, which can be obtained by exfoliating the bulk WS₂ into its corresponding sheets [5]. However, obtaining micro- and nano-scale WS₂ systems was not easy due to lack of availability of a standard, cost-effective and user-friendly

route in spite of numerous efforts. Earlier, nanoscale WS₂ systems were synthesized using methods, such as chemical vapour deposition, magnetron sputtering, laser ablation, etc. [6], all of which come with much sophistication and with a need for high temperature. Synthesizing nanoscale WS₂ *via* a hydrothermal route does not require very high temperature processing and could offer products with less or no agglomeration, phase homogeneity and good crystallization [7]. Moreover, a surfactant-assisted hydrothermal route was also employed to fabricate WS₂ nanostructures [8].

In this work, we report on the processing of WS₂ nanosheets using a facile, hydrothermal route followed by effective ultrasonication. Morphological, photocatalytic and nitrogen adsorption–desorption properties were highlighted along with the scope for future investigation.

2. Experimental

2.1 Synthesis procedure and steps

First, a single-step hydrothermal process is attempted for the production of WS₂ and consequently, exfoliated into its nanosheets form with the help of repeated ultrasonication. The chemicals used in the synthesis were of analytical grade and were used without further purification. For synthesis, sodium tungstate (Na₂WO₄ · 2H₂O) (Rankem, 98% pure) was used as the source of tungsten, and thiourea (CH₄N₂S)

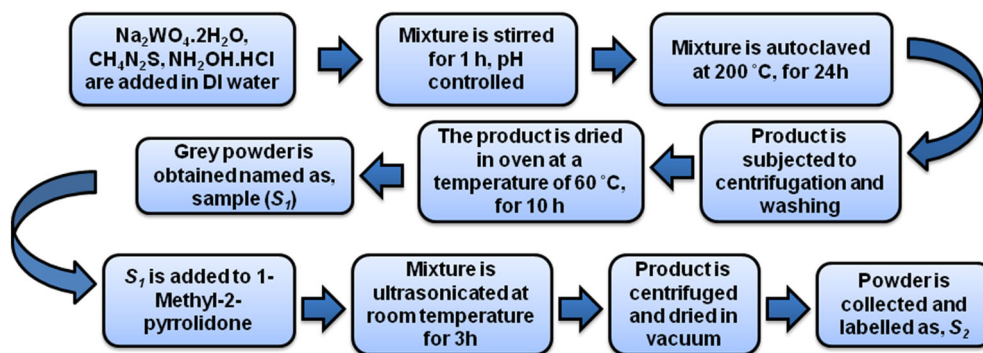


Figure 1. The block diagram of steps involved for synthesizing WS₂ nanosheets.

(Merck, 99% pure) for sulphur. In a typical synthesis, 1.65 g of sodium tungstate, 0.72 g of hydroxylamine hydrochloride (NH₂-OH · HCl) (Merck, 98% pure) and 1.17 g of thiourea were dissolved in 30 ml of deionized Millipore[®] water. The solution was stirred for 1 h until a clear solution is obtained, while maintaining the solution at pH = 6. The mixture was then transferred into a 50 ml Teflon-lined autoclave, and upon proper sealing, it was kept in oven at a temperature of 200 °C for 24 h. After allowing it to cool naturally, the obtained product was washed several times with deionized water and ethanol, and employed centrifugation (~4000 rpm) for 10 min. The precipitate was oven-dried at a temperature of 60 °C and consequently, a dark grey-coloured powder is acquired. The synthesized powder was labelled as S₁.

To obtain nanosheets out of the synthesized WS₂ powder, 0.2 g of the powder was added to 20 ml of 1-methyl-2-pyrrolidone (Merck, 99.5% pure) and then, subjected to ultrasonication bath (UD100SH: $f = 50$ Hz, $P = 100$ W) for 4 h. The solution was then centrifuged (~5000 rpm) for 10 min and two-third of the solution was considered for further centrifugation (~7000 rpm) for 15 min, followed by multiple washing with ethanol. The as-received precipitate was collected and then oven-dried (~60 °C) for 10 h. The resulting product that yielded WS₂ nanosheets was labelled as S₂. The whole synthesis steps are highlighted in a block diagram shown in figure 1.

2.2 Characterization techniques employed

To exploit the structural and crystallographic properties, X-ray diffraction (XRD) technique was employed using a Bruker AXS, Germany D8 focus X-ray diffractometer equipped with a CuK_α source ($\lambda = 1.543$ Å). The morphological detail of the as-synthesized WS₂ nanosheets is revealed through both scanning electron microscopy (SEM; JEOL JSM, 6390LV) and transmission electron microscopy (TEM; FEI, Tecnai) imaging studies. The compositional analysis was performed through the energy-dispersive X-ray (EDX) spectroscopy studies. On the other hand,

phonon-assisted vibrational modes are studied through the Raman spectrometer (Renishaw, Wotton-under-Edge) using a Ar⁺ laser ($\lambda = 514$ nm line) as the excitation source. Information regarding nanosheet-surface area, pore size and pore distribution were evaluated through the Bruner-Emmet-Teller (BET, Quantachrome Nova 1000e, FL) analysis performed on the WS₂ nanosheets by way of studying N₂ adsorption/desorption response at liquid nitrogen temperature (~77 K). UV-Vis spectroscopy (UV 2450, Shimadzu Co.) study was employed to obtain energy gap as well as photocatalytic degradation efficiency.

2.3 Execution of photocatalytic experiment

To analyse the photocatalytic efficiency of the as-prepared WS₂ sheets, we have chosen malachite green (MG) as the target to be decomposed. MG is an organic compound that is used as a dye-stuff (triaryl methane dye) and controversial antimicrobial agent in aquaculture [9]. Recognized as class II health hazard, researchers are trying hard to find means to degrade these harmful dyes found in sea foods and pigment industry. The photoactivity of the nano-WS₂ samples was investigated both under UV and visible light illumination conditions. To perform the experiment, 60 mg l⁻¹ of the WS₂ nanoparticles is first added to 20 mg l⁻¹ of the MG, and then subjected to stirring for about 1 h in dark, then, the mixture is ultrasonicated for about half an hour. The collected solution is then placed inside a cabinet, which has the provision for UV lamp as well as the incandescent bulb, the latter being used as the source of visible light. The samples are kept at the base of the chamber and at a distance of about 12 cm from the UV source ($\lambda = 365$ nm) and the polychromatic light source used independently. The WS₂ nanocatalyst-loaded dyes are irradiated for different time durations: 15, 30, 45 and 60 min. Next, 5 ml of the MG solution is employed for the optical absorption analysis, knowing that the peak maximum for the initial absorption of MG normally appears at ~619 nm [10]. The percentage of decomposition of the target MG under

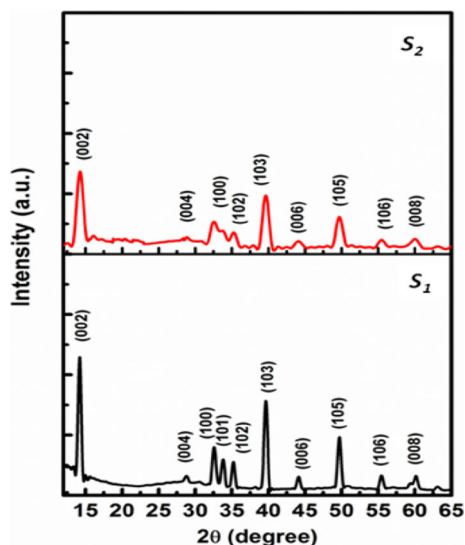


Figure 2. XRD patterns of un-exfoliated WS₂ (S₁) and exfoliated WS₂ nanosheets (S₂).

UV and visible light illuminations can be evaluated through the formula:

$$\% \text{ Degradation} = \frac{C_0 - C_t}{C_0} \times 100\%, \quad (1)$$

where C₀ and C_t represent concentration of MG solution before and after irradiation [11].

3. Results and discussion

3.1 Structural and morphological analysis

Figure 2 shows the XRD patterns of the as-prepared WS₂ samples (un-exfoliated and nanosheets). The samples exhibit diffraction peaks at nearly same positions and no shift in the peak position was observed. The diffraction peaks positioned at 2θ = 28.76, 32.66, 33.42, 35.26, 39.57, 44.28, 49.65, 55.53 and 60.31 correspond to (004), (100), (101), (102), (103), (006), (105), (106) and (008) planes of the hexagonal (H) structure of WS₂, respectively [7]. The prominent peak located at 2θ = 14.38° signifies the (002) plane of 2H-WS₂ (JCPDS file no. 08-0237). The remarkable difference between the XRD patterns of the two samples is in the intensity of the peaks with the nanosheets possessing a relatively lower value due to lack of adequate atomic planes participating in the diffraction process. The lowering of the peak intensity is attributed to the decrease in crystallinity of the nanosheet as compared to the un-exfoliated WS₂ powder [12]. The diffraction peaks in the XRD pattern of WS₂ sheets are also tend to get broadened, which suggests the exfoliation of the WS₂ powder into the sheets of nanoscale form [13]. No peak either due to impurities or oxide phase was witnessed in the diffractograms, thus, indicating the formation of the phase-pure WS₂ product in this case.

The micrographs of the un-exfoliated (S₁) and nanosheet (S₂) WS₂ powder captured on a HRSEM machine are shown

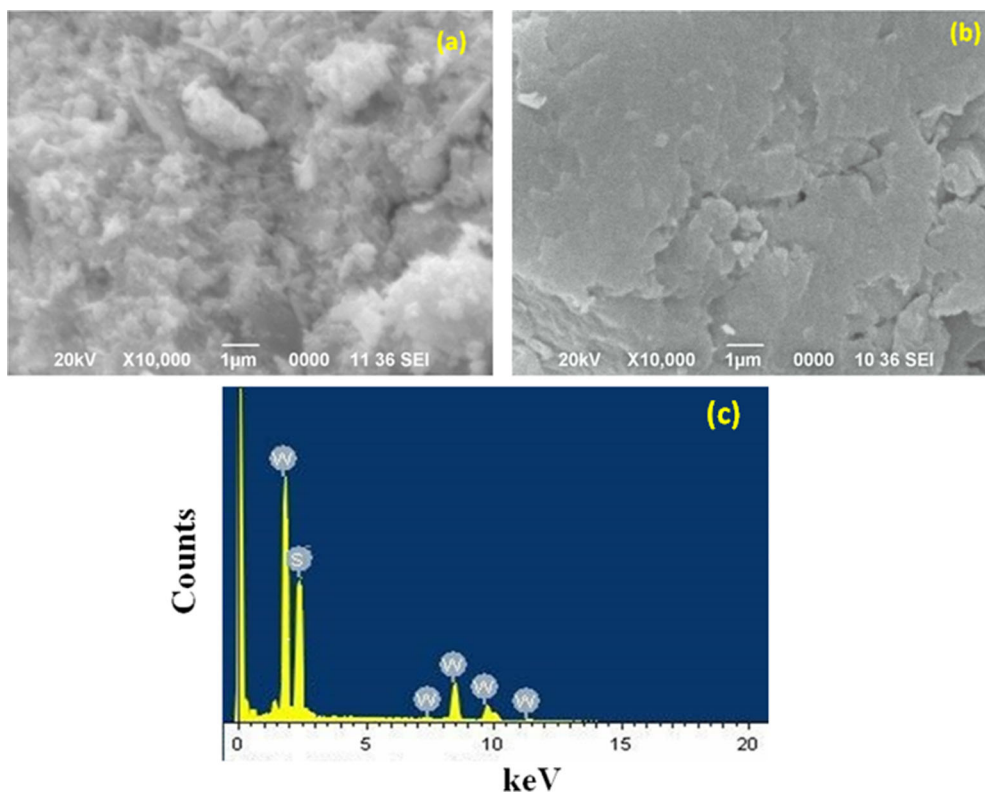


Figure 3. The SEM micrograph of (a) un-exfoliated WS₂ powder and (b) exfoliated WS₂ nanosheets. (c) The EDX micrograph of the un-exfoliated WS₂ powder.

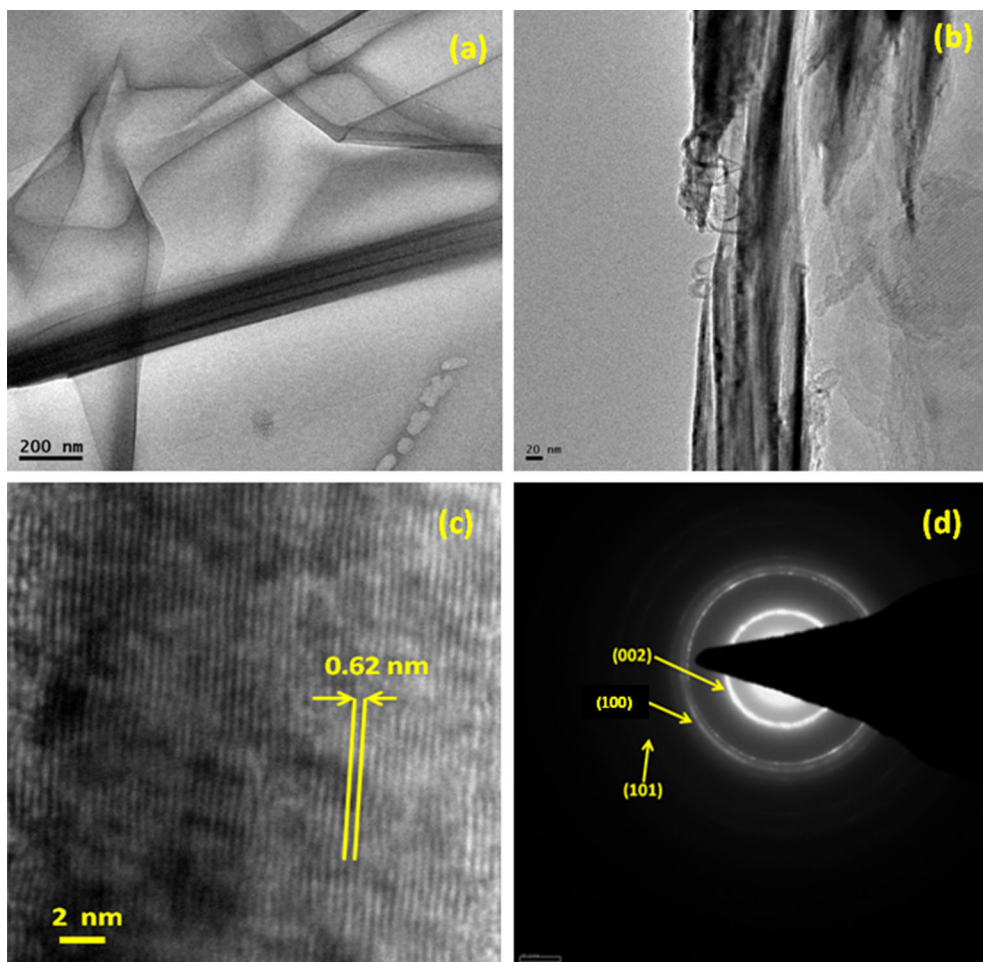


Figure 4. TEM micrograph of (a) WS₂ nanosheets, (b) magnified view of the sheets, (c) lattice fringe pattern captured at the surface and (d) SAED pattern indicating diffused diffraction rings.

in figure 3a and b, respectively. Figure 3b shows the EDX micrograph of the as-synthesized WS₂ powder. The presence of the elements W and S can be clearly seen in the EDX spectrum. Intensity-based calculations gave the ratio of S to W to be 1.90:1. Moreover, the exfoliated sheets are visualized at a higher magnification through TEM imaging (figure 4a, b). The nanosheets indicating a higher surface area coverage can be noticed with a few kinks and folds. The lattice fringe pattern captured at the edge of the WS₂ nanosheets is shown in figure 4c. Using ImageJ software[®] [14], the average fringe width defining lattice spacing of the nanosheets was calculated to be ~ 0.62 nm. Moreover, the observation of diffused ring like patterns is an indicative of the polycrystalline content present in the synthesized WS₂ product (figure 4d).

3.2 Optical absorption response and Raman active vibrational features

In the optical absorption spectra shown in figure 5, two absorption peaks located at 536 and 633 nm can be observed for the un-exfoliated WS₂ system (*S*₁). The absorption peak at

536 nm is ascribed to the transitions from spin-split valence band to the conduction band [15], whereas the peak at 633 nm corresponds to *d-d* type transitions at the centre of the Brillouin zone [16]. The corresponding peaks are blue-shifted to 519.6 and 620.7 nm on exfoliation as observed for the nanosheets (*S*₂). Earlier, the blue-shifting of the absorption peaks was viewed as a consequence of quantum confinement effect [16]. Consequently, the optical band gap would increase for the exfoliated WS₂ nanosheets, as compared to its un-exfoliated form. Moreover, the second peak is effectively suppressed for the nanosheets owing to a lowered value of *d-d* transitional probability.

Figure 6 highlights the Raman spectra of the as synthesized WS₂ systems. Apparently, two distinct peaks corresponding to the *E*_{2g}¹ and *A*_{1g} Raman active modes can be seen [17]. The *E*_{2g}¹ mode represents an in-plane optical mode, whereas the *A*_{1g} mode signifies the out-of-plane vibrations of the sulphur atoms [18]. We also noticed a small blue-shifting in the Raman peaks from 351.26 (417.32) to 356.07 (421.66) cm⁻¹, as *S*₁ was converted to *S*₂ through exfoliation.

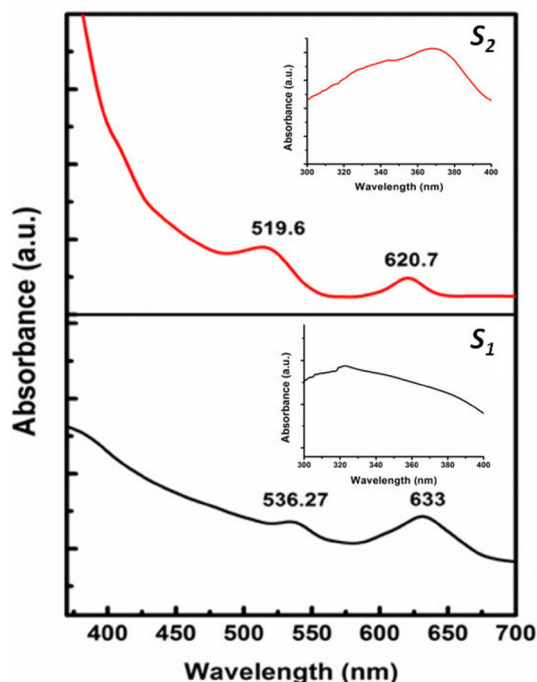


Figure 5. UV-Vis optical absorption spectra of the (S_1) un-exfoliated WS_2 powder and (S_2) exfoliated WS_2 nanosheets.

The exfoliation causes a weak layer interaction, leading to an appreciable peak shifting towards higher wavenumber [19]. The ratio of the intensities of the E_{2g}^1 and A_{1g} peaks was calculated to be 0.68 for the nanosheets, which is comparatively higher than the bulk WS_2 [20]. A blue shift of Raman peaks was observed in case of the nanosheets as compared to the un-exfoliated WS_2 , owing to phonon confinement effect.

3.3 Photocatalytic activity of WS_2 nanosheets on MG dye

The photocatalytic performance of the WS_2 nanosheets is examined on a harmful organic dye (MG). The extent of degradation was observed under both UV and visible light illumination and for different durations of time. With an increase in time duration of the UV exposure, the WS_2 nanosheet-loaded dye showed a steady fall in the absorption response at $\lambda = 619$ nm (figure 7A (a-c)). We also observed a rapid fall in the absorbance under visible light illumination (figure 7A (d-f)). In other words, the WS_2 nanosheets tend to exhibit a better catalytic efficiency under visible light. This is because of its narrow band gap, which acts as a facilitator to activate the redox reaction necessary for the production of hydroxyl radicals, which play a vital role in the photocatalytic activity. A scheme illustrating photocatalytic activity of WS_2 nanosheets is shown in figure 7B and the mechanism as detailed below.

Upon light irradiation, the WS_2 nanosheets are believed to be photo-excited releasing electrons and holes. The electrons are lifted to the conduction band leaving behind holes in the

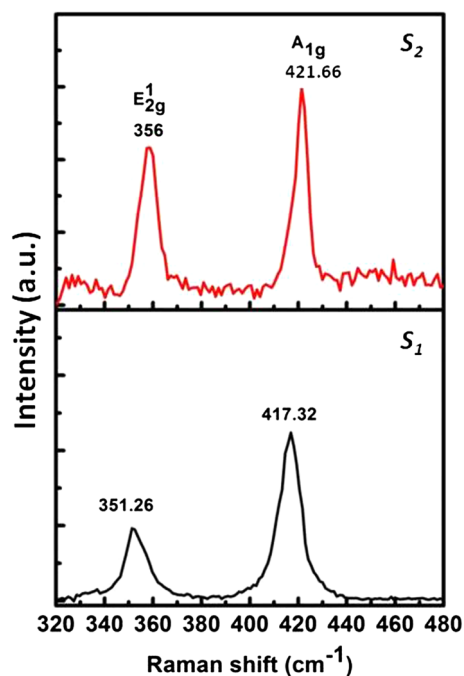


Figure 6. Raman spectra of the (S_1) un-exfoliated WS_2 nanopowder and (S_2) exfoliated WS_2 nanosheets.

valence band. The e-h pairs are likely to be captivated in the active W^{4+} and S^{2-} defect sites, otherwise, it is likely that recombination of these carriers would take place to dissipate energy [21]. These carriers would migrate to the nanocatalyst surfaces, resulting in the formation of intermediate reactants. The light-induced holes and the reactive hydroxyl radicals are extremely important for the stimulation of the redox reaction necessary for decomposition of water. The target MG, being in aqueous form, the water molecule is believed to come in contact with the surfaces of the nanocatalyst. The active sites of the nanocatalyst readily trap the OH group, or superoxide O_2^- , latter being a consequence of the electrons being transferred to the adsorbed oxygen [22]. Water and hydroxyl groups are transformed to hydroxyl radicals by the photo-generated holes. The superoxide and hydroxyl radicals are readily responsible for the decomposition of the organic dyes into harmless entities [23].

The characteristic photocatalytic features shown in figure 7A (a-f) suggest an increase in photodegradation of the MG with irradiation time duration, notably, for an exposure time of 60 min. The WS_2 nanosheets under UV illumination gives a 67.4% decomposition of MG. But visible light could decompose as high as 86.6% of the MG dye. In a recent work, we have discussed the photodegradation activity of the inorganic fullerene (IF) type WS_2 nanoparticles, which exhibited 45 and 71.2% degradation of the dye under respective illumination conditions, but for a larger duration of time [21]. Thus, the photoactivity of the WS_2 nanosheets, owing to its relatively high specific surface area, is drastically enhanced. A higher surface area with mesopores would allow

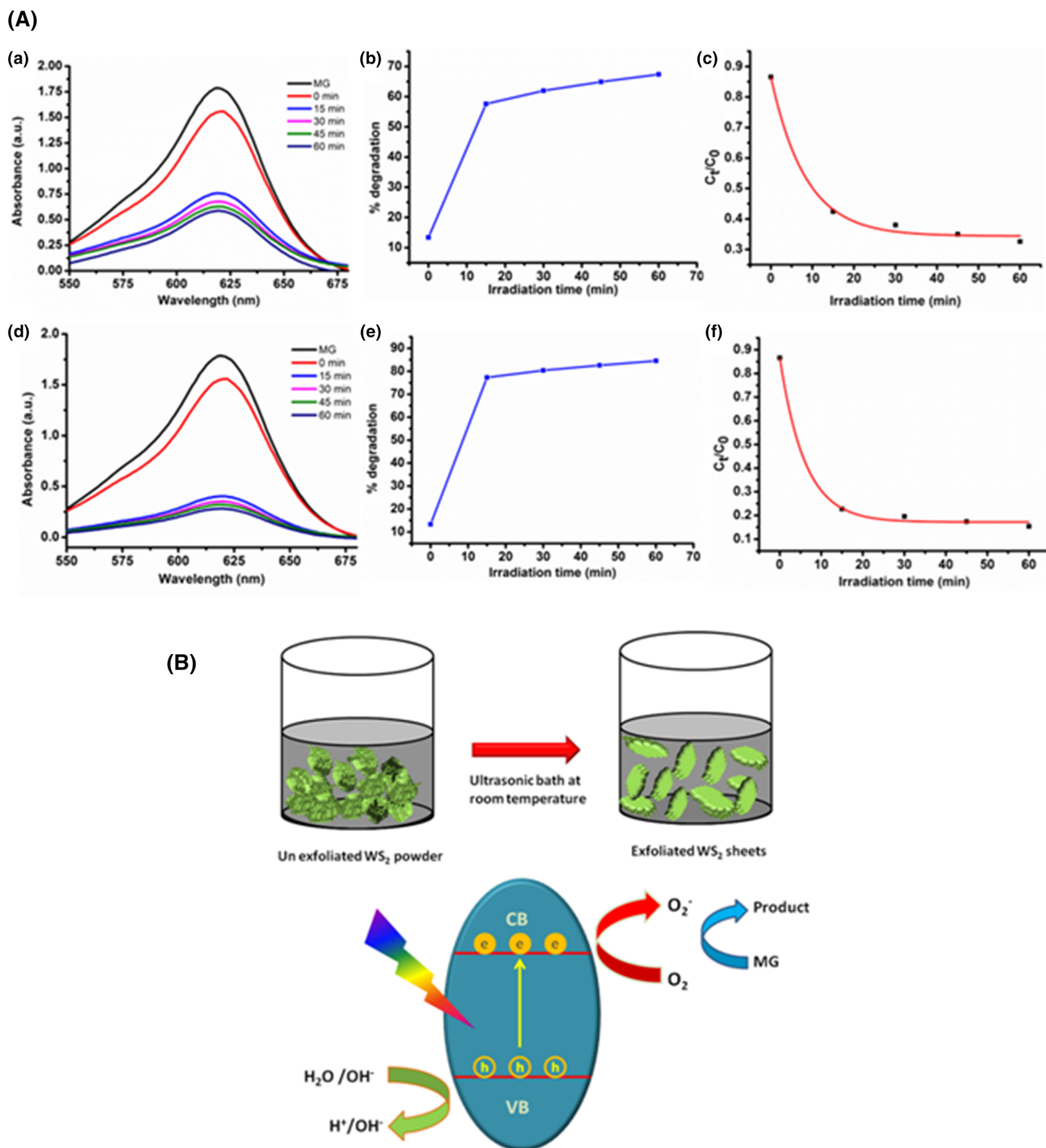


Figure 7. (A) UV–Vis optical absorption spectra of MG and WS₂ nanocatalyst (nanosheet)-loaded dye with different irradiation times, percentage of photodegradation and pseudo-first-order plots: (a–c) UV light illumination and (d–f) visible light illumination. (B) The schematic diagram representing the formation of nanosheets and the mechanism of photocatalysis.

more MG molecules to get adsorbed into the active sites under visible light irradiation. The performance of the UV illumination is relatively less due to the band gap excitation led possibility of photo-oxidation at the pores and interfaces. The kinetics of photocatalytic degradation of MG at the nanocatalyst (WS₂ nanosheets) surface can be evaluated qualitatively

by employing a simple Langmuir–Hinshelwood (L–H) model [24].

It can be expressed in the form of a first-order reaction for a dilute solution (mM) ($C \ll 1$):

$$C_t = C_0 e^{-k_r t}, \quad (2)$$

where C_0 is the initial concentration of the MG solution, t the illumination time and k_r the pseudo-first-order rate constant.

At $t = 0$, one obtains where $C_t = C_0$, the initial concentration of the target before irradiation. The degradation trends of the MG dye can be found in figure 7A (b and e). Similarly, the curves of C_t/C_0 vs. t for different exposure conditions are shown in figure 7A(c and f). The exponential decay trend would help to determine the pseudo-first-order rate constant, k_r involved in the reactions under UV and visible light illuminations. The k_r values are estimated as, 0.11 and 0.16 min^{-1} , respectively. An improved rate constant under visible light exposure suggests an improved photoactivity owing to induction of maximal redox reaction at the nanosheet surfaces through release and participation of free carriers, formation of superoxide radicals, etc. Moreover, the possibility of photo-oxidation is largely avoided in this case, as compared to the UV photo-excitation condition.

3.4 BET surface area and pore-size analysis using N_2 adsorption–desorption curve

Surface analysis of nanoscale materials is an important aspect as it offers sound information regarding surface coverage and particularly, specific surface area, pore size, pore volume, etc. In this regard, earlier N_2 adsorption and desorption isotherms were employed for studying mesoporous WS_2 [25]. The type of isotherm is identified as type IV profile, which is the characteristic of a mesoporous material with pore diameter typically in the range of 2–50 nm [26]. Essentially, adsorption on mesoporous solids occurs *via* multilayer adsorption phenomena mediated *via* capillary condensation that results in type IV and V isotherms [27]. Here, figure 8 represents the characteristic N_2 adsorption/desorption isotherm of our hydrothermally processed and exfoliated WS_2 nanosheets. The initial part of the type IV isotherm is attributed to monolayer–multilayer adsorption, since it follows the same trend as the

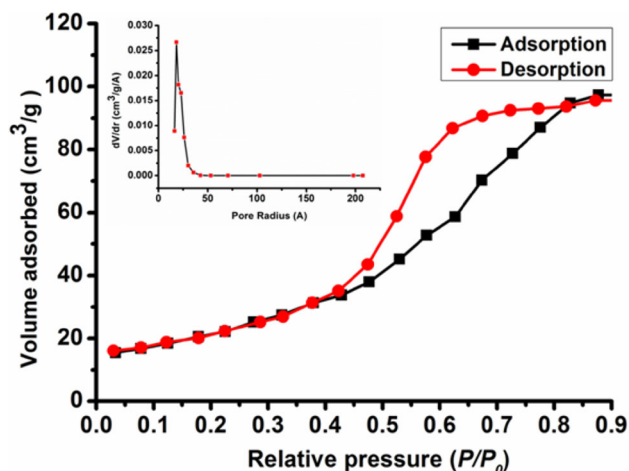


Figure 8. The nitrogen gas adsorption–desorption curve of the WS_2 nanosheets. The BJH pore size distribution curve is shown as inset.

corresponding part of a type II isotherm obtained with the given adsorptive on the same surface area of the adsorbent in a nonporous form. The hysteresis loop is appeared to be of the type H2 according to IUPAC classification, which indicates disordered distribution of pore size and shape. The hysteresis loop is found to occur at a magnitude above ~ 0.5 of relative pressure P/P_0 . The BJH pore-size distribution graph for the same sample is shown in the inset of figure 8. The BET surface area of the nanosheets is found to be $211.5 \text{ m}^2 \text{ g}^{-1}$. Using the BJH model, the pore volume and the average size of the pores are evaluated to be 0.433 cc g^{-1} and 3.8 nm , respectively.

The Kelvin's equation [28] is:

$$\ln \frac{P}{P_0} + \frac{4\gamma V_m}{dRT} = 0, \quad (3)$$

where P and P_0 represent actual and saturated vapour pressures, V_m molar volume, γ the surface tension of liquid N_2 and $d (=2r, r$ being radius) the size of the droplet. The symbols R and T signify universal gas constant ($8.31 \text{ J mol}^{-1} \text{ K}^{-1}$) and working temperature (77 K); respectively. Applying the respective values, we obtain the diameter of the drop that desorb out of the pores as $d = 2r = 2.1 \text{ nm}$. However, a relatively larger pore size ($2r \sim 3.8 \text{ nm}$) predicted through the experimental analysis and shown as inset of figure 8, might have arisen due to the existence of interconnected pores on the surfaces of the nanosheets. Earlier we also predicted similar pore sizes in case of nanoscale TiO_2/PbS network [29].

4. Conclusion

We have demonstrated spectroscopic, photocatalytic and sorption characteristics of WS_2 nanosheets derived through a hydrothermal route and exfoliation. While possessing a hexagonal crystal structure, the nanosheets exhibited a lattice spacing of 0.63 nm . Raman measurement on the WS_2 nanosheets has revealed E_{2g}^1 and A_{1g} modes with an intensity ratio of ~ 0.68 , which is higher than its value for the bulk counterpart. The BET N_2 adsorption–desorption curve gives a type-IV pattern with an open hysteric feature. Exhibiting a high specific surface area, the nanosheets are believed to have mesopores with an average pore dimension of $\sim 3.8 \text{ nm}$. Moreover, the photodegradation of the MG dye under visible light illumination was seen to be more effective than under UV light condition. The band gap excitation led photo-oxidation might hinder the redox reactions at the nanocatalyst surface sites in the latter case. More analysis with inclusion of C-dots [30] and also emphasizing on irradiation aspect is in progress.

Acknowledgements

We acknowledge IUAC, New Delhi, for the financial support (Project: UFR-56322/2014 and 62312/2017). The

initial assistance of Ms Mayuri Bora during experimental work is acknowledged. Further, we thank SAIC, Tezpur University, for extending several analytical facilities.

References

- [1] Chhowalla M, Shin H S, Eda G, Li L-J, Loh K P and Zhang H 2013 *Nat. Chem.* **5** 263
- [2] Wang Q H, Kalantar-Zadeh K, Kis A, Coleman J N and Strano M S 2012 *Nat. Nanotechnol.* **7** 699
- [3] Tenne R 2006 *Nat. Nanotechnol.* **1** 103
- [4] Mishra A K, Lakshmi K V and Huang L 2015 *Sci. Rep.* **5** 15718
- [5] Vattikuti S V P, Byon C and Reddy Ch. Venkata 2016 *Mater. Res. Bull.* **75** 193
- [6] Tang G, Tang H, Li C, Li W and Ji X 2011 *Mat. Lett.* **65** 3457
- [7] Shang Y, Xia J, China Zhude Xu and Chen W 2005 *J. Disp. Sci. Technol.* **26** 635
- [8] Cao S, Liu T, Hussain S, Zeng W, Peng X and Pan F 2014 *Mat. Lett.* **129** 205
- [9] Srivastava S, Sinha R and Roy D 2004 *Aquat. Toxicol.* **66** 319
- [10] Rabieh S, Bagheri M, Heydari M and Badiei E 2014 *Mater. Sci. Semicond. Process.* **26** 244
- [11] Paul N, Deka A and Mohanta D 2014 *J. Appl. Phys.* **116** 144902
- [12] Mao X, Xu Y, Xue Q, Wang W and Gao D 2013 *Nanoscale Res. Lett.* **8** 430
- [13] Lin H, Wang J, Luo Q, Peng H, Luo C, Qi R *et al* 2017 *J. Alloys Compd.* **699** 222
- [14] <http://imagej.nih.gov/ij/>
- [15] Ghorai A, Bayan S, Gogurla N, Midya A and Ray S K 2017 *ACS Appl. Mater. Interfaces* **9** 558
- [16] Nguyen T P, Choi S, Jeon J-M, Kwon K C, Jang H W and Kim S Y 2016 *J. Phys. Chem. C* **120** 3929
- [17] Nguyen T P, Sohn W, Oh J H, Jang H W and Kim S Y 2016 *J. Phys. Chem. C* **120** 10078
- [18] Molina-Sanchez A and Wirtz L 2011 *Phys. Rev. B: Condens. Matter* **84** 155413
- [19] Le Q V, Nguyen T P and Kim S Y 2014 *Phys. Status Solidi RRL* **8** 390
- [20] Berkdemir A, Gutiérrez HR, Botello-Méndez Andrés R, Perea-López Néstor, Elías Ana Laura, Chia C-I *et al* 2013 *Sci. Rep.* **3** 1755
- [21] Hazarika S J and Mohanta D 2017 *Appl. Phys. A* **123** 381
- [22] Bingham S and Daoud W A 2011 *J. Mater. Chem.* **21** 2041
- [23] Peng T, Zhao D, Song H and Yan C 2005 *J. Mol. Catal. A* **238** 119
- [24] Gaya U I and Abdullah A H 2008 *J. Photochem. Photobiol. C* **9** 1
- [25] Vattikuti S V and Byon C 2015 *Sci. Adv. Mater.* **7** 2639
- [26] Alothman Z A 2012 *Materials* **5** 2874
- [27] Kruk M and Jaroniec M 2001 *Chem. Mater.* **13** 316
- [28] Butt H-J, Graf K and Kappl M 2006 *The Kelvin equation: physics and chemistry of interfaces* (Weinheim: Wiley-VCH)
- [29] Dutta N, Mohanta D and Choudhury A 2011 *J. Appl. Phys.* **109** 094904
- [30] Hazarika S and Mohanta D 2019 *J. Luminescence* **206** 530



Excitation dependent light emission and enhanced photocatalytic response of WS₂/C-dot hybrid nanoscale systems

Saurabh J. Hazarika, Dambarudhar Mohanta*

Nanoscience and Soft Matter Laboratory, Department of Physics, Tezpur University, PO: Napaam, Tezpur 784028, Assam, India



ARTICLE INFO

Keywords:

TMDC
C-dot
Hydrothermal
Excitation
Emission
Photocatalytic

ABSTRACT

A facile, hydrothermal route has been employed to synthesize two dimensional (2D) WS₂ nanosystems, followed by decoration with C-dots derived from the orange juice extract as the source of carbon. Imaging through transmission electron microscopy (TEM) reveals the formation of C-dots on the WS₂ sheets, with dot size varying between 2 and 5 nm and *d*-spacing of 0.31 nm. The WS₂/C-dot hybrid nanosystems were found to reveal excitation dependent luminescence response with underlying mechanism attributed to the influence of either surface traps or/and prevalent heteroatoms. Moreover, Raman spectra of the nano hybrid exhibited both in-plane optic and out of plane vibronic modes, positioned at $\sim 352.8 \text{ cm}^{-1}$ (E_{2g}^1) and 421.7 cm^{-1} (A_{1g}); apart from two additional peaks, assigned to the *D* and *G* bands of the graphitic material. Finally, photocatalytic degradation of methyl orange (MO) and malachite green (MG) were studied under visible light illuminations. While exhibiting a comparatively stronger photoactivity, the MG dye yielded degradation efficiency as high as, $\sim 83\%$ and 91% in case of use of bare WS₂ nanosheet and WS₂/C-dots as nanocatalysts; respectively. The bifunctional candidates would find a special place in advanced material research owing to exhibition of enhanced radiative emission as well as photocatalytic features.

1. Introduction

Tungsten disulfide (WS₂), a member of the transition metal dichalcogenide (TMDC) family, has drawn significant research interest owing to its immense potential in the field of microelectronics, optoelectronics, catalysis and solid lubrication [1]. Like graphene, WS₂ comes with a two dimensional (2D) layered structure, which is capable of exhibiting a sizable band gap that can also be tuned [2]. Because of the atomically layered structure, it has got large surface- to- volume ratio and thus, enriched with numerous reactive sites [3]. As a result, it could serve as an efficient photocatalyst while considering degradation of harmful pollutants and dyes. Researchers have explored the photocatalytic performance of WS₂ in different morphologies and also in composite form with other suitable candidates [4,5]. In the past, there has always been some effort to enhance the photocatalytic efficiency of WS₂, MoS₂ and related compounds [4–7]. Apart from photocatalytic activity, WS₂ also offers a broad visible luminescence response [8].

It is a general perception that, radiative recombination emission and photocatalytic activity occur via opposite mechanisms, so both cannot be enhanced simultaneously. Typically, the C-dots are a new class of carbon nanomaterials with a size of less than 10 nm. As compared to the traditional semiconductors, carbon dots (C-dots) are superior in terms

of solubility, chemical inertness, biocompatibility and photo-emission property [9–11]. Moreover, the C-dots are capable of exhibiting both size and excitation wavelength dependent photoluminescence (PL) property [9]. The C-dots also show very good photocatalytic response, both in individual and composite forms [12]. The broad light sensing response of C-dots could stimulate the charge separation process which helps in stabilizing semiconductor photocatalysts. Atkin et.al have synthesized C-dots in the already prepared 2D WS₂ nanosystems by employing a conventional microwave technique followed by a detailed study on photocatalytic degradation of Congo Red (CR) using the as-derived hybrid system as the nanocatalyst [13].

In this work, we highlight synthesis and physical properties of WS₂/C-dot hybrid nanosystems. In contrast to the processing of 2D WS₂ nanosheets by a facile, hydrothermal route followed by ultrasonication, the C-dots were obtained via a green route, considering orange juice as the source of carbon. The mechanism of formation of C-dots from orange juice involves hydrothermal carbonisation of the major constituents, such as, sucrose, glucose, fructose, citric acid and ascorbic acid [14]. Apart from Raman and photoluminescence characteristics, photocatalytic activity of the WS₂/C-dot hybrid nanosystem is being discussed on select, harmful dyes under visible light irradiation.

* Corresponding author.

E-mail address: best@tezu.ernet.in (D. Mohanta).

<https://doi.org/10.1016/j.jlumin.2018.10.019>

Received 28 June 2018; Received in revised form 29 September 2018; Accepted 3 October 2018

Available online 11 October 2018

0022-2313/ © 2018 Elsevier B.V. All rights reserved.

2. Experimental: materials and methods

The description about materials, protocol and techniques employed are as detailed below.

2.1. Synthesis of tungsten disulfide (WS_2) nanopowder

A facile, hydrothermal route has been employed for the production of WS_2 nanopowder. In a typical experiment, 1.65 g of sodium tungstate ($Na_2WO_4 \cdot 2H_2O$; Rankem, 98% pure), and 1.52 g of thiourea (CH_4N_2S ; Merck, 99% pure) were dissolved in 30 ml of deionized (DI) water. Latter, 0.72 g of hydroxylamine hydrochloride ($NH_2OH \cdot HCl$; Merck, 98% pure) is added to the aforesaid solution. The mixture was kept under constant stirring (~ 300 rpm) for about 1 h, with pH adjusted to 6 by dropping a few ml of hydrochloric acid (HCl). The sol was then transferred into a 50 ml teflon-lined stainless steel autoclave, sealed properly and latter placed in an open air oven at a temperature of $200^\circ C$, for 24 h. The autoclaved product was collected and then washed several times with DI water and with AR grade ethanol under high speed centrifugation ($\sim 10,000$ rpm). The residue was then dried in vacuum oven kept at a temperature of $70^\circ C$, for 10 h. The obtained product offered a bluish grey appearance.

2.2. Processing of WS_2 nanosheets from its powder

The as prepared WS_2 nanopowder is converted to 2D sheets via ultrasonication. At first, 0.2 g of WS_2 nanopowder was ground and added to 20 ml of 35% ethanol solution. The sol is then sealed in a closed vial and subjected to ultrasonication (50 kHz) for nearly 120 min. The supernatant is collected in an eppendorf after the sol was subjected to centrifugation (~ 1500 rpm), for 10 min. This was centrifuged (~ 3500 rpm) further for a time duration of 30 min. Subsequently, the resulting supernatant is carefully removed and kept as the finished product.

2.3. Preparation of 2D- WS_2/C -dot hybrid nanosystems

Following an earlier work [14], in a typical process, 20 ml of matured orange juice (absolutely pulp-free) was mixed with 15 ml ethanol in a beaker. First, a mixture of 10 ml of the as collected WS_2 supernatant and 10 ml of the clean orange juice was transferred into a 50 ml teflon-lined stainless-steel autoclave. After sealing airtight, the autoclave was subjected to heating at a constant temperature of $120^\circ C$, for about 2 h. After the reaction is over, the autoclave was allowed to cool down naturally. As a result, a yellowish colored sol is obtained, which exhibited bluish green fluorescence under UV excitation. A schematic block diagram illustrating synthesis steps can be found in Fig. 1.

2.4. Characterization techniques

To exploit the structural and crystallographic properties of the WS_2 nanopowder, X-ray diffraction (XRD) technique was employed using a MiniFlex Rigaku X-ray diffractometer equipped with a CuK_α source ($\lambda = 1.543 \text{ \AA}$). Moreover, the elemental composition of the product under study has been confirmed through the EDX analysis. The morphological details of the as-synthesized WS_2/C -dot nanosystem were revealed through transmission electron microscopy (FEI, Tecnai) imaging studies. On the other hand, luminescence characteristics and phonon-assisted vibrational modes were exploited through the fluorescence spectrophotometer (Hitachi F-2700) and Raman spectrometer (Chemlogix, EZRaman-N); respectively. The optical absorption spectra, as obtained through the UV-Vis spectrophotometer (UV 2450, Shimadzu Corporation) were used for estimating optical band gap as well as photocatalytic degradation efficiency.

2.5. Execution of photocatalytic experiments

In order to analyze the photocatalytic degradation efficiency, we opted malachite green (MG) and methyl orange (MO) as the targets and WS_2/C -dot hybrid system as the nano-catalyst. The MG is an organic compound that is used as a dyestuff and controversially, as an anti-microbial agent in aquaculture [15]. In contrast, the MO dye is regarded as a pH indicator in the titration process because of its precise color variance with pH. While researchers across the globe putting numerous effort to tackle associated problems due to harmful dyes and pollutants, there is no short cut to address the critical issues. Consequently, advanced materials are always welcome in this area of technological interest.

The photoactivity of the WS_2/C -dot nanohybrid has been investigated after subjected to visible light illumination. First, 0.7 mg of the MG dye and an equal amount of MO dye were separately added to 50 ml of the 35% ethanol solution. Under constant stirring for about 1 h in the dark, 6 ml of the as prepared WS_2/C -dot solution was added to the stirred mixture. In the next step, the mixture was ultrasonicated for about half an hour. The collected sol was then placed inside a closed cabinet under visible light source. In this set up, the samples under study were placed on the base of the chamber, located at a vertical distance of 12 cm from the visible lamp (Philips, 15 W). The WS_2/C -dot nanocatalyst loaded dye was irradiated under visible light for about 0, 15, 30, 45, 60 min. Next, 5 ml of the MG and MO solutions were taken for optical analysis knowing that, the peak maxima for the initial absorption of the MG appeared at ~ 617 nm, and for MO located at ~ 456 nm [16,17]. In presence of the nano-catalyst, the percentage of decomposition of the MG and MO under visible light illumination for different time durations of the visible light exposure can be assessed through the following relation:

$$\% \text{ degradation} = (C_0 - C_t)/C_0 \times 100,$$

where, C_0 and C_t represent absorbance maxima of the nano-catalyst loaded dye solution before and after irradiation. It may be noted that, a suppression of the absorption response would indicate a proportionate lowering of the dye concentration in presence of the nanocatalyst.

3. Results and discussion

Physical properties as regards, morphological, vibrational, photoluminescence and photocatalytic responses of WS_2/C -dot nanohybrids are as discussed below.

3.1. Structural and morphological analyses

Fig. 2(a) depicts powder x-ray diffractogram (XRD) of the synthesized WS_2 nanosheets. As can be noticed, the most intense diffraction peak is located at the Bragg's angle, $2\theta = 14.40^\circ$, which corresponds to the (002) plane of the hexagonal WS_2 . The other diffraction peaks at $\sim 28.87^\circ$, 32.58° , 33.41° , 35.97° , 39.49° , 44.75° , 49.80° , 55.36° are attributed to the respective crystallographic planes indexed as, (004), (100), (101), (102), (103), (006), (105) and (106) of the hexagonal WS_2 system (JCPDS File No. 08-0237) [18].

Fig. 2(b-d) essentially characterizes a set of the SEM micrographs of the WS_2 nanosheets, captured at low and high magnifications. Several folds and kinks can be clearly witnessed in the WS_2 nanosheets. The elemental composition is ascertained from the EDX spectrum of the WS_2 nanosystem, shown as inset of Fig. 2(a). The presence of W and S elements is quite evident from the spectrum along with a Cu peak that might arise from the Cu-grid used to hold the specimen under study. Fig. 3(a-c) shows a number of TEM micrographs of the as prepared 2D WS_2/C -dot nanohybrid specimen in order of increasing magnifications. Apparently, the C-dots were observed to spread over the nanosheets of WS_2 (Fig. 3(a-c)). On the other hand, the lattice fringe patterns could be revealed at higher magnifications (Fig. 3(d, e)). The interplanar spacing

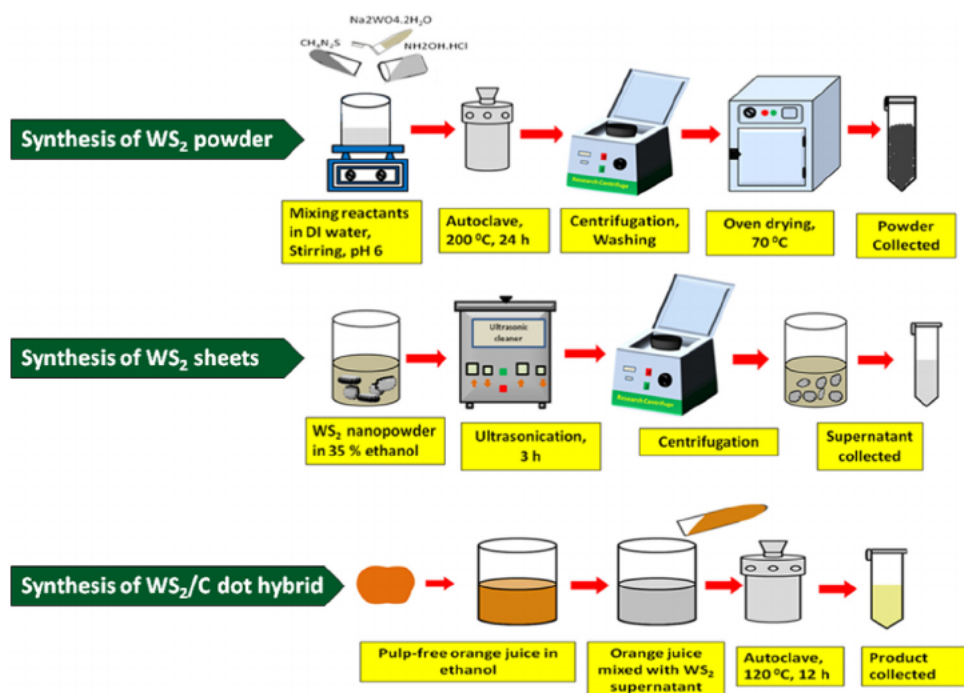


Fig. 1. Schematic block diagram of the synthesis steps for processing WS₂ nanopowder, nanosheets and WS₂/C-dot hybrid nanosystems.

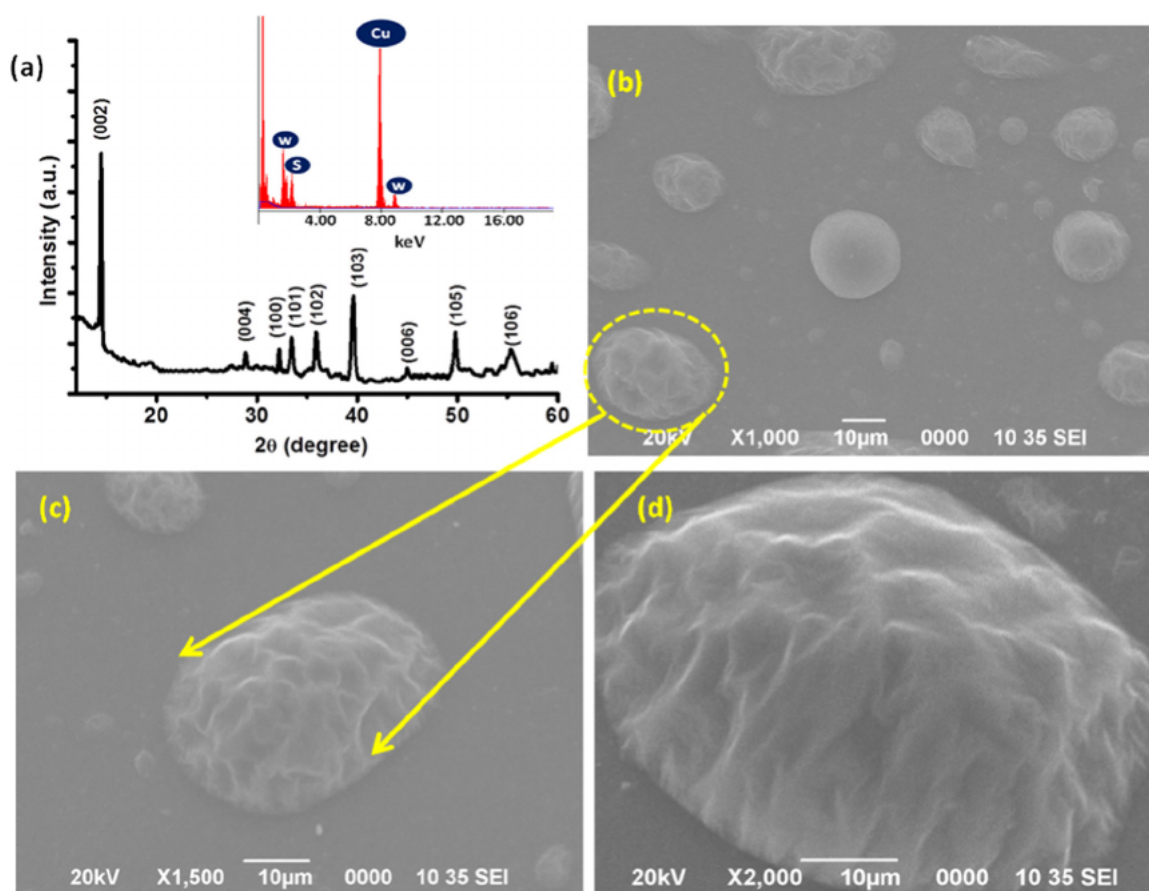


Fig. 2. (a) X-ray diffractogram and (b-d) scanning electron micrographs of the synthesized nano-WS₂ system. Note the sheets with folds and kinks at higher magnifications. The EDX spectrum is shown as inset in (a).

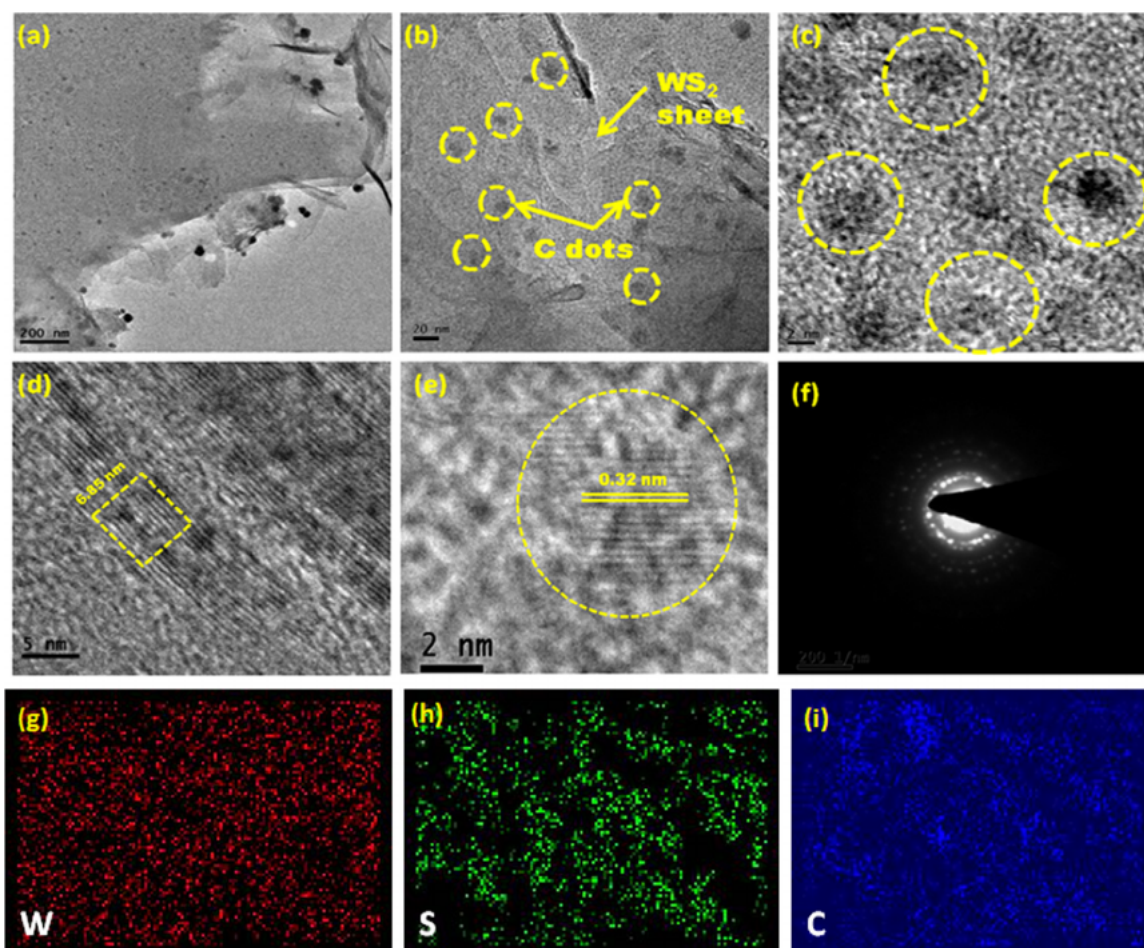


Fig. 3. TEM images of (a) nano-WS₂ with C-dots at low magnification, (b) WS₂/C-dot nanohybrid at a higher magnification, and (c) an enlarged view of the isolated C-dots. Information with regard to lattice fringe patterns of the WS₂ and C-dot systems can be noticed in (d) and (e), respectively. The SAED pattern highlighting diffused rings is shown in (f). Whereas, elemental mappings of the WS₂/C-dot nanohybrid can be found in (g-i).

of the WS₂ nanosheet, as measured with the help of using *ImageJ*[®] software is approximately, 0.62 nm. Moreover, the C-dots are found to be nearly spherical, with size varying in the range 2–5 nm, and with an approximate *d*-spacing of 0.34 nm. The C-dots are fairly uniform in size and are seen to spread all over the 2D plane of the WS₂ nanosheets, without being agglomerated. The diffused rings, found in the SAED pattern indicate polycrystalline nature of the specimen under study (Fig. 3(f)). The images which illustrate elemental mapping of the WS₂/C-dot specimen, are shown in Fig. 3(g-i). It essentially depict visual indication about distribution of relevant elements W, S and C present in the specimen. For the sake of clarity, the elemental signals were generated independently in a specific area and assigned with a distinct color pattern.

3.2. Probing Raman active modes

Raman spectroscopy is an important, yet versatile tool to identify Raman active modes in a given specimen. Moreover, extensive analysis is capable of providing information as regards, number of layers, nature of defects, doping levels, microstrain and other useful details. Fig. 4(a) represents the Raman spectra of the synthesized nano-WS₂ system measured at an excitation wavelength, $\lambda_{\text{ex}} \sim 785$ nm. The WS₂ nanosheets showed two major vibronic bands, E_{2g}^1 and A_{1g} modes, which are located at ~ 350 cm⁻¹ and 420.3 cm⁻¹; respectively [13]. These modes essentially correspond to the in-plane optical mode and out-of-plane vibrational modes of the sulfur atoms within the nano-system [13]. For clarity, a zoomed in version of these peaks are shown in

Fig. 4(b). Relative to WS₂ only nano-system, the E_{2g}^1 and A_{1g} Raman active modes of the WS₂/C-dot nanohybrid are shifted marginally toward higher frequency side by approximately, 2.83 cm⁻¹ and 1.40 cm⁻¹, respectively. Moreover, the E_{2g}^1 -to- A_{1g} intensity ratio of the nanohybrid system, experienced a marginal improvement from a value of 0.70 to a value of 0.79. Also, the full width at half maxima (FWHM) of the modes gets improved substantially (Table 1). The overall feature is ascribed to the strong interaction between the C-dots and WS₂ nanosheets, which can strengthen both in-plane and out-of-plane effective restoring forces acting on them [19]. Furthermore, emergence of two additional peaks located at ~ 1335.7 cm⁻¹ and 1531 cm⁻¹ are assigned to the D and G bands of the graphitic content [20]. While the D band corresponds to the defects existing in the graphitic carbon material, the G band is linked to the sp^2 carbon atoms in the graphitic layers [21]. Since the G-band appears due to stretching of C-C bonds in the sp^2 bonded material, the asymmetric nature might have arisen due to the presence of unsaturated bonds at the adjoining interface of WS₂ and C-dots. Upon de-convolution (not shown), the G-band was seen to offer three superimposed peak maxima, positioned at ~ 1519.8 cm⁻¹, 1551.7 cm⁻¹ and 1595.9 cm⁻¹.

3.3. Optical absorption and excitation dependent luminescence feature

The UV–visible optical absorption spectra of both WS₂ nanosheets and 2D WS₂/C-dot nanohybrid samples are depicted in Fig. 5(A)(a). It may be noted that, C-dots were not prepared separately rather, processed in a precursor containing WS₂. Accordingly, absorption and

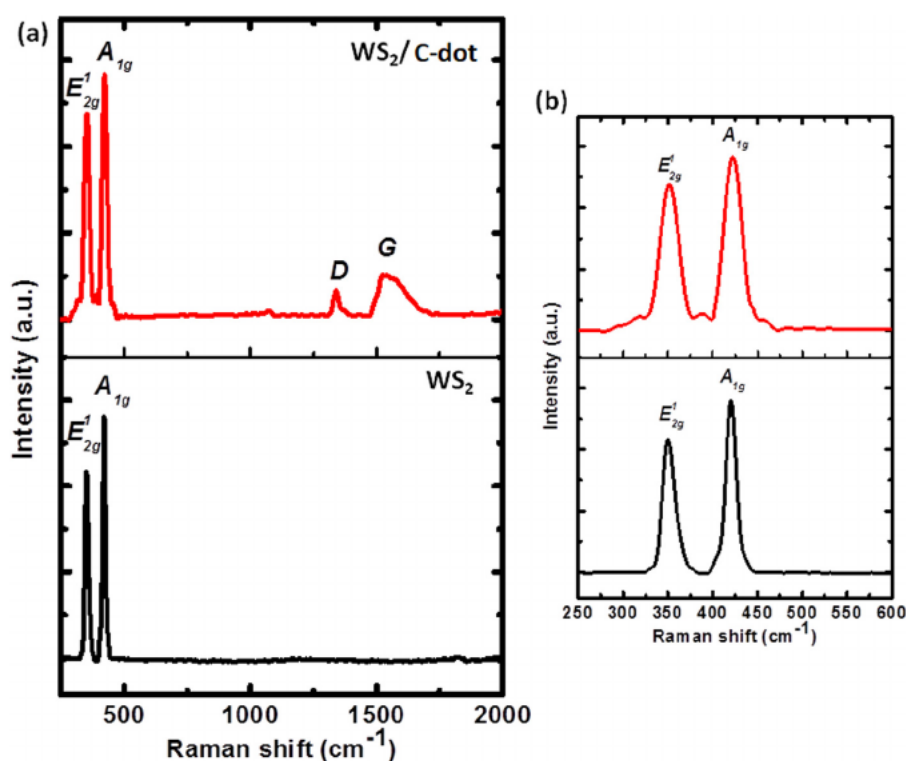


Fig. 4. (a) Raman spectra of the WS₂ nanosheet and WS₂/C-dot nanohybrid systems. The magnified views of the E_{2g}¹ and A_{1g} modes are highlighted in (b).

Table 1

Raman spectra analysis of WS₂ and WS₂/C-dot nanoscale systems.

Sample	Raman modes	FWHM (cm ⁻¹) E _{2g} ¹ ; A _{1g}	Intensity ratio (E _{2g} ¹ /A _{1g})
WS ₂ nanosheet	E _{2g} ¹ and A _{1g}	16.45; 13.59	0.70
WS ₂ /C-dot nanohybrid	E _{2g} ¹ and A _{1g} ; D and G (graphitic)	23.54; 22.62	0.79

photoluminescence responses of the hybrid WS₂/C-dot system is compared with the WS₂ only system. The absorption band at ~ 632 nm corresponds to the *d-d* type transitions of the WS₂ at the center of the Brillouin zone [22]. The absorption band at ~525 nm is ascribed to the transitions arising from the spin-split valence band to the conduction band [23], and the band located at ~450 nm may arise from the localized density of states (DOS) existing between the valence and conduction bands [23]. The absorption spectrum of the WS₂/C-dot hybrid system, however, gave multiple peaks: ~ 270 nm, 295 nm, 450 nm, 520 nm and 630 nm. In fact, the C-dots are known to exhibit broad UV absorption at ~ 295 nm, which is the characteristic peak of carbon rich nanoparticles synthesized by way of carbonization of chitosan [24]. Fig. 5(A)(b) represents the corresponding PL spectra under an excitation wavelength of λ_{ex} = 360 nm. As can be noticed, the hybrid WS₂/C-dot nanosystem gives a much improved luminescence response due to enriched radiative property of the C-dots behaving like fluorophore. Since the PL spectra of the WS₂ nanosheet and WS₂/C-dot hybrid systems share the similar line-shape, one can anticipate relevant surface interaction between the WS₂ nanosheets and the C-dots in the hybrid system. Moreover, the digital snap shots of the cuvette containing WS₂/C-dot nanohybrid specimen and captured under white and UV light illuminations, can be found in Fig. 5(A)(c). To be specific, the yellow colored specimen under visible light turns blue under UV light exposure.

A series of excitation wavelength dependent PL spectra of the WS₂/C-dot hybrid system are shown in Fig. 5(B)(a). For 3D plots, please refer to Supplementary document. When the excitation wavelength (λ_{ex}) is changed from 350 nm to 440 nm, the corresponding PL emission peaks

(λ_{em}) seem altered with the central maxima varying between ~450 nm (blue) and 531 nm (green). Moreover, we also noticed a small emission peak at ~714 nm corresponding to λ_{ex} = 560 nm, shown as inset in Fig. 5(B)(a) (See also Supplement). As a general trend, with the increase in the excitation wavelength, the PL emission intensity first improves and then, gets weakened substantially. However, the up-converted PL property of the C-dots, which is reported to be an important reason to improve the photocatalytic activity of such kind of hybrid cannot be ensured in this case [25]. The PL excitation spectra, were acquired at fixed emission wavelengths, and shown in Fig. 5(B)(b).

At present, there is no clear cut mechanism available to justify excitation dependent luminescence in layered systems. However, in graphene quantum dots and its derivatives, different groups have advocated excitation dependent luminescence as a consequence of quantum size effect, giant red-edge effect, surface trap and heteroatoms [26]. In our case, we expect the latter mechanisms to be mainly responsible for displaying excitation dependent PL features. The surface traps model essentially relies on adequate trap states due to the oxygen rich groups, such as, -COOH and -OH available at the surface of the C-dots. The availability of continuous yet different localized defect states can account for the PL emissions at different wavelengths [26–28]. On the other hand, electronegativity of heteroatoms model suggests that, surface active groups and heteroatoms may influence the PL response of the C-dots significantly. The fluorescence peak would experience red-shifts when C-dots are doped with S or Se, which act as electron donors owing to their low electronegative character [26]. Since the WS₂ nanosheets are evolved with ample dangling bonds, when anchored with the C-dots the latter might be crowded with free S-atoms at the

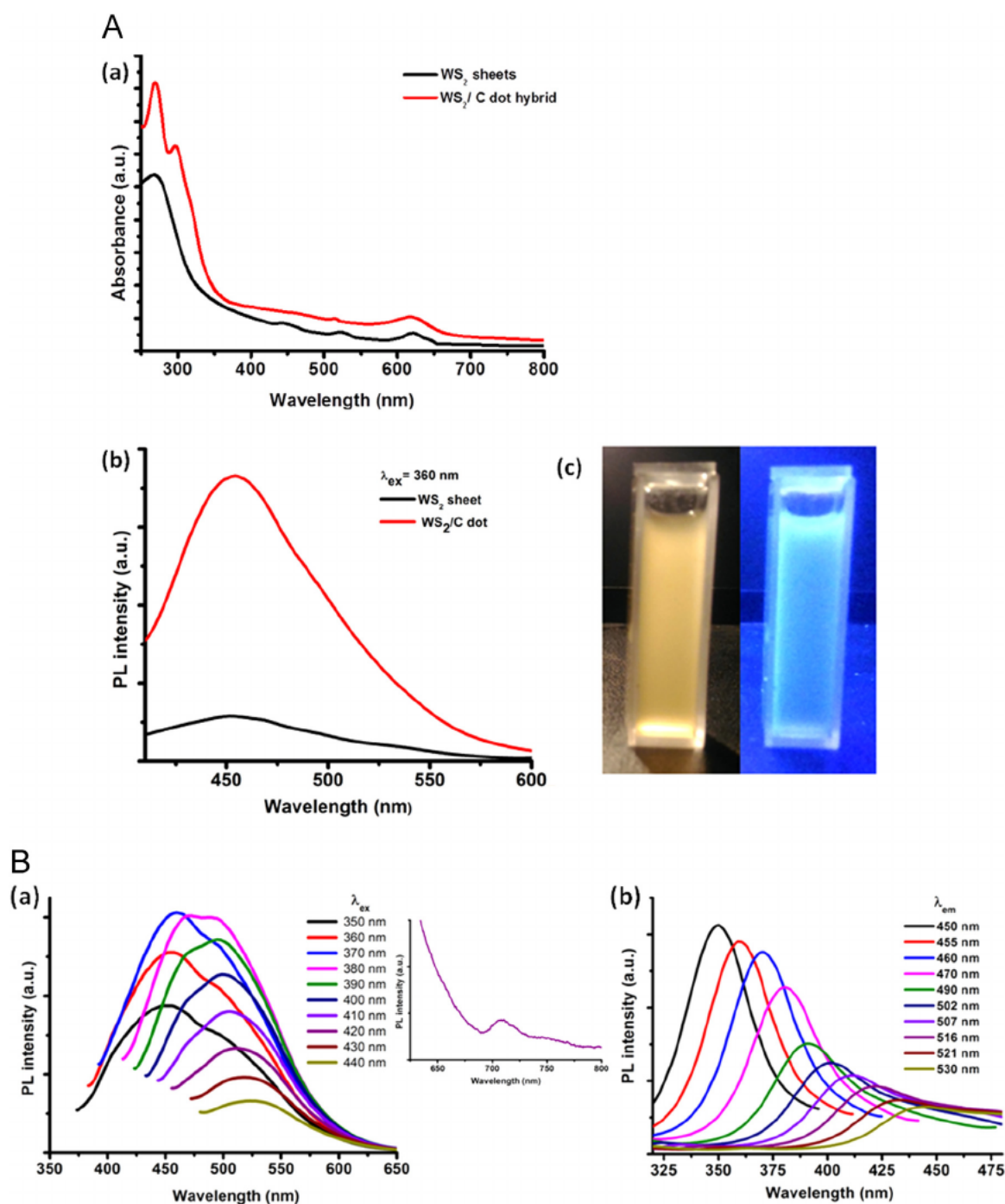


Fig. 5. A: (a) UV–visible optical absorption and (b) PL emission spectra ($\lambda_{\text{ex}} = 360$ nm) of the synthesized WS_2/C dot nanosystems. Digital photographs captured under visible and UV light exposure of the cuvette containing nanohybrid specimen, are shown in (c). B: A series of (a) excitation dependent PL emission spectra and that of (b) PL excitation spectra of the WS_2/C -dot nanosystem. Since excitation at $\lambda_{\text{ex}} = 560$ nm gives a weak emission peak at $\lambda_{\text{em}} = 714$ nm, it is shown independently as figure inset of (a). C: The fluorescence micrographs under different excitation source: (a) white, (b) UV, (c) blue, and (d) green.

interface. Consequently, C-dots would realize edge doping with S and can become responsible for the excitation dependent red shifting in the PL spectra [26,29]. In order to substantiate excitation dependent response, fluorescence microscopy was also employed to exploit fluorescent nature of the synthesized WS_2/C -dot nanosystem, images being shown in Fig. 5(C)(a-d). Apparently, the images exhibited brown, blue, green and red impressions, when the nanohybrid specimen was excited with white, UV, blue and green light; respectively. Note the well dispersed bright spots in each case, which are believed to have arisen from the surface anchored C-dots spread over the WS_2 nanosheets.

3.4. Photocatalytic activity on harmful organic dyes

In order to investigate photoactivity of the as-synthesized WS_2/C -dot hybrid system, we have chosen MO and MG dyes as the target agents (See also Supplement) under visible light illumination and considering different time duration of light exposure. To draw insight from the photoactivity contribution arising due to the C-dots, experiment was conducted first on bare WS_2 nanosheets [30] and then on WS_2/C -dot nanohybrid systems. The UV–Vis optical absorption responses of the organic dyes and the nanocatalyst-loaded MO and MG

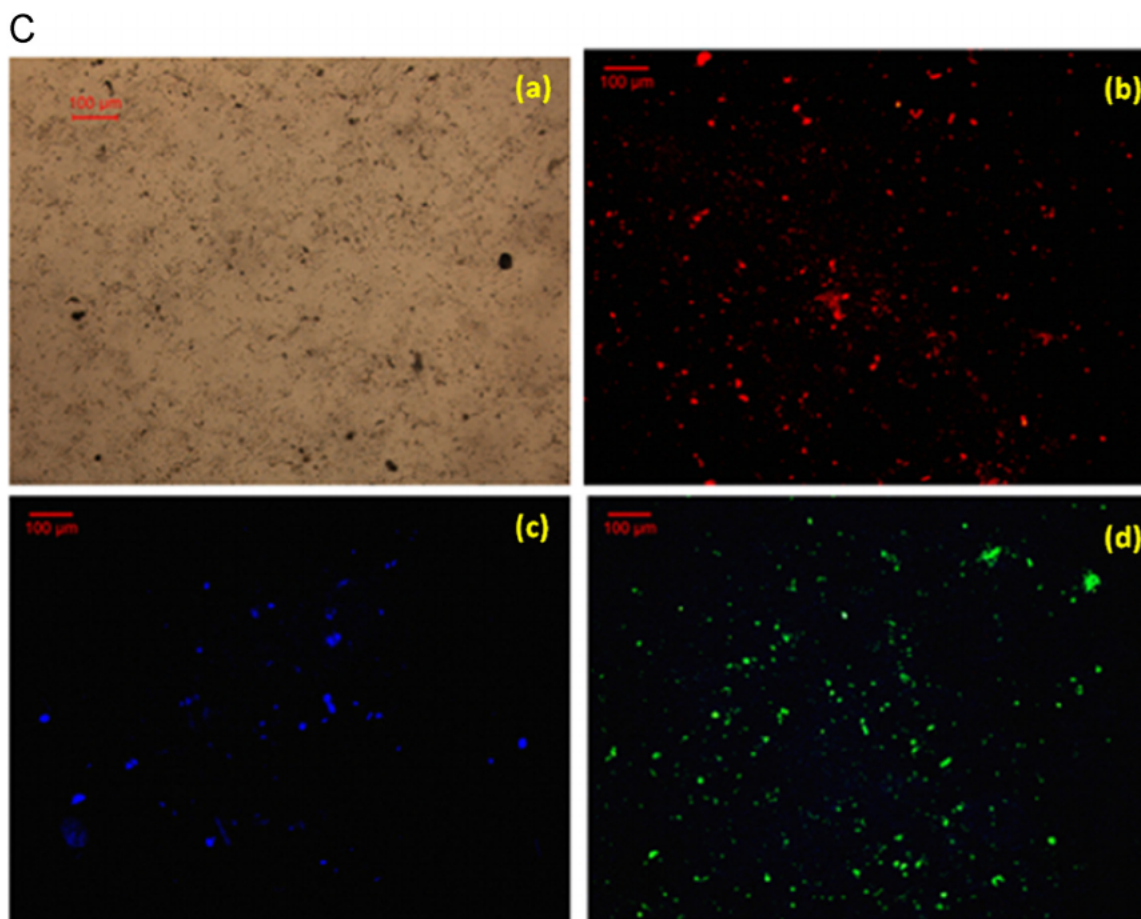


Fig. 5. (continued)

systems can be found in Fig. 6A and 6B (col.1). Recognizing untreated MO and MG peak maxima at ~ 456 nm and ~ 617 nm, as can be noticed, the absorbance shows a steady fall with increasing exposure time. Whereas, MO characterizes a broad spectral feature, MG gave a steep spectral response. Qualitatively, when exposed to visible light for a time duration of 60 min, we obtained respective photodegradation efficiency of $\sim 72.3\%$ and 83.2% for the MO and MG dyes with inclusion of bare WS_2 nanosheets as photocatalyst (Fig. 6A, col.2). However, the degradation efficacy of the MO and MG dyes, in presence of WS_2/C -dot nanocatalyst was estimated to be, $\sim 81.2\%$ and 91% ; respectively (Fig. 6B, col.2). Moreover, the photodegradation response was seen to be much rapid in case of MG than the case for MO dye, possibly because of its strong sensitivity to the red part of the visible light (Fig. 6, col. 2). In our recent works on inorganic fullerene (IF) type and nanosheet-based WS_2 systems, we acquired the MG degradation efficiency as high as, 71% and 86% when subjected to visible light illumination [30,31]. The WS_2/C -dot nanohybrid system, has thus shown an apparent increment in the photocatalytic activity. The C-dots play an important role in enhancing the photoactivity of the 2D WS_2 , which can be explained by the physisorption process of the dye onto the WS_2 flakes [13]. Several environmental and chemical applications have been reported based on the physisorption of organic aromatics onto graphene systems [32,33]. Normally when photons are incident on the WS_2 surfaces, the electrons are excited to the conduction band leaving aside the holes in the valence band. The deficiency of electron in the valence band of WS_2 can be filled by an incoming electron from the HOMO level of the dyes, which are in close proximity to the hybrid system [13]. As the process continues, the decomposition of the dye would take place until thermodynamic equilibrium is achieved. The schematic illustration for the degradation mechanism is shown in Fig. 6(C)(a,b).

The photocatalytic degradation mechanism can be understood by using a simple kinetics. Employing simple kinetics on the photodegradation of MO and MG dyes at the nanocatalyst surfaces, one can implicitly use Langmuir–Hinshelwood (L-H) model to assess rate constants [34]. For a dilute solution (mM) ($C \ll 1$), it can be expressed in the form of a first-order reaction given by [34]: $C_t = C_0 e^{-k_a t}$, here, C_0 is the initial concentration of either MO or MG solution, t is the irradiation time and k_a is the pseudo-first-order rate constant. The rate constant essentially describes the rate of photoactivity of the nanocatalyst for a given target. Moreover, at $t = t_0$, $C_t = C_0$, the initial concentration before irradiation. The nature of plots of C_t/C_0 versus t , are shown in Fig. 6A and 6B (col. 3). The plots essentially help to predict the pseudo-first-order rate constant, k_a . To be specific, a higher rate constant predicts a higher amount of degradation of the target dye. The rate constants, as directly obtained from the nature of the curves and using the above equation, are estimated to be, 0.012 min^{-1} and 0.058 min^{-1} when MO and MG dyes were loaded with WS_2 nanosheets; respectively. In contrast, WS_2/C -dot loaded MO and MG systems gave respective k_a values as, 0.0215 min^{-1} and 0.168 min^{-1} . Apparently, the WS_2/C -dot nanohybrid is extremely sensitive to photoactivity as compared to its bare nanosheet counterpart.

4. Conclusion

Hydrothermally synthesized 2D WS_2 nanosheets, decorated with C-dots have been processed and characterized emphasizing PL and photocatalytic activity. TEM images revealed the formation of 2–5 nm sized C-dots spread over the WS_2 nanosheets. The synthesized WS_2/C -dot nanohybrids were found to exhibit excellent fluorescence property, highly tunable with the excitation wavelength. The PL spectra of the

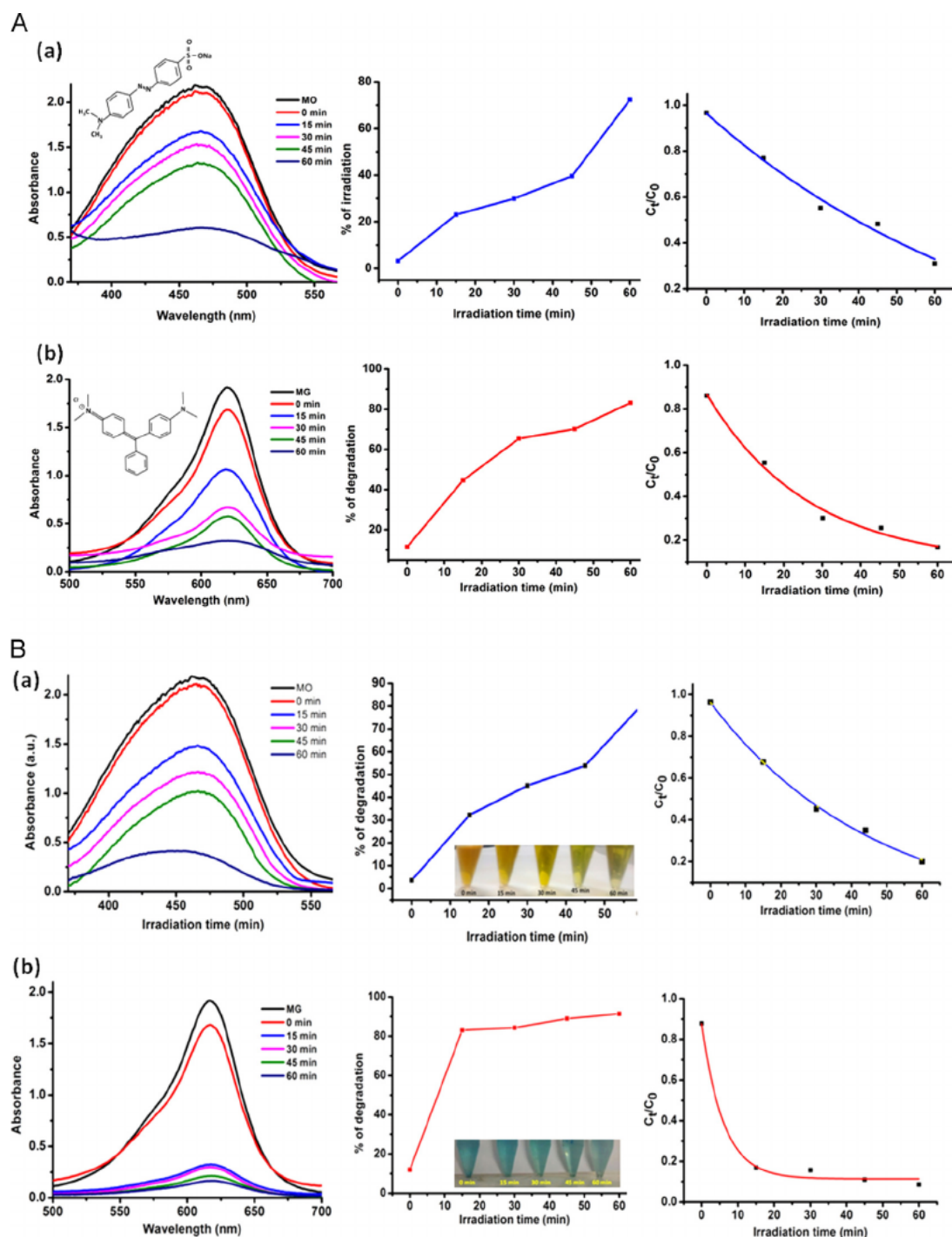


Fig. 6. A: Optical absorption spectral features illustrating photodegradation of (a) MO and (b) MG dyes under visible light illumination and using WS_2 nanosheets as the desired nanocatalyst. The exact nature of degradation with exposure time can be found in col.2 and col.3. B: Optical absorption spectral features illustrating photodegradation of (a) MO and (b) MG dyes under visible light illumination and using WS_2/C -dots as the desired nanocatalyst. The exact nature of degradation with exposure time can be found in col.2 and col.3. C: Schematic illustration of the photocatalytic activity: (a) degradation mechanism and (b) relevant energy scheme.

WS_2/C -dot hybrid system displayed an overall rise, because of the presence of the fluorophore like C-dots. The underlying mechanism for exhibition of excitation dependent PL and red-shifting response has been attributed to models related to surface traps and electronegativity of heteroatoms. Moreover, as compared to the WS_2 nanosheets, the Raman spectrum of the WS_2/C -dots hybrid nanosystem offered a marginal shifting of both the in-plane optic and out of plane vibronic modes, namely, E_{2g}^1 and A_{1g} ; toward lower frequency side along with the evolution of two additional peaks, assigned to the D and G bands of

the graphitic system. Finally, using the synthesized nanocatalysts, photocatalytic degradation of MO and MG dyes were examined under visible light illumination. The degradation efficiency as high as, ~81.2% and 91% could be achieved against the respective target-dyes after an exposure time duration of 60 min. An enhanced radiative emission and photocatalytic responses would uncover deep insight which needs further investigation in this direction.

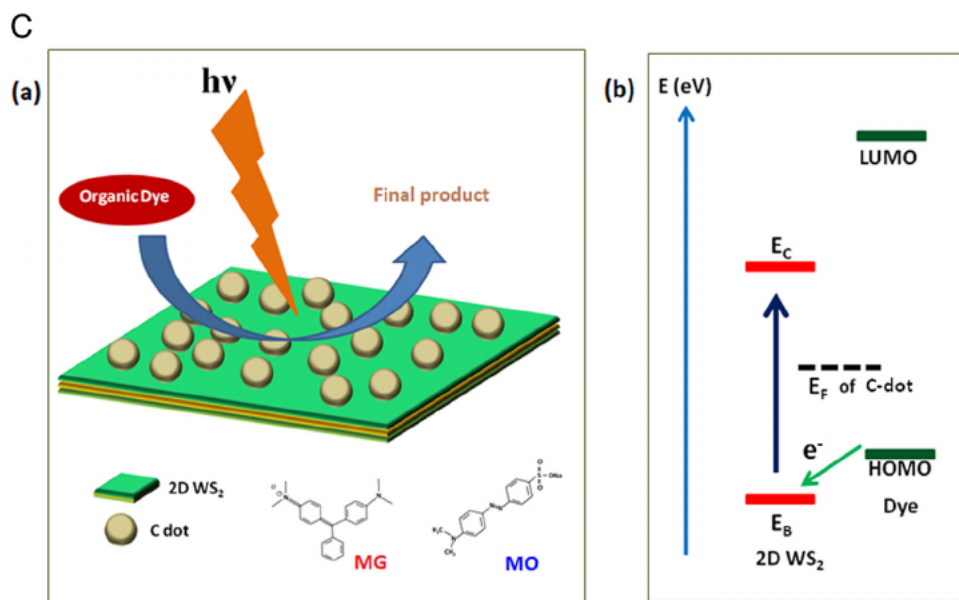


Fig. 6. (continued)

Acknowledgments

We extend our sincere thanks to IUAC, New Delhi for the financial support (UFR: 56322/2014 and 62312/2017). We also acknowledge CSIR, New Delhi for sanctioning a project (No. 03(1448)/18/EMR-II) recently. We thank SAIC, Department of Physics and Department of Chemical Sciences, TU for extending various characterization facilities. We are thankful to Mr. Kiranjyoti Mohan and Nabadeep Chamuah for their help in carrying out the PL and Raman characterizations; respectively. We also acknowledge timely assistance received from Mr. Manash Jyoti Nath.

Appendix A. Supplementary material

Supplementary data associated with this article can be found in the online version at doi:10.1016/j.jlum.2018.10.019.

References

- [1] A. Eftekhari, Tungsten dichalcogenides (WS₂, WSe₂, and WTe₂): materials chemistry and applications, *J. Mater. Chem. A* 5 (2017) 18299.
- [2] Q.H. Wang, K.K. Zadeh, A. Kis, J.N. Coleman, M.S. Strano, Electronics and optoelectronics of two-dimensional transition metal dichalcogenides, *Nat. Nanotechnol.* 7 (2012) 699–712.
- [3] B. Peng, P.K. Ang, K.P. Loh, Two-dimensional dichalcogenides for light-harvesting applications, *Nano Today* 10 (2015) 128.
- [4] Y. Sang, Z. Zhao, M. Zhao, P. Hao, Y. Leng, H. Liu, From UV to Near-Infrared, WS₂ nanosheet: A novel photocatalyst for full solar light spectrum photodegradation, *Adv. Mater.* 27 (2) (2015) 363–369.
- [5] J. Low, S. Cao, J. Yu, S. Wageh, Two-dimensional layered composite photocatalysts, *Chem. Commun.* 50 (2014) 10768–10777.
- [6] P. Liu, Y. Liu, W. Ye, J. Ma, D. Gao, Flower like N-doped MoS₂ for photocatalytic degradation of RhB by visible light irradiation, *Nanotechnology* 27 (2016) 225403.
- [7] Nan Tian, Z. Li, D. Xu, Y. Li, W. Peng, G. Zhang, F. Zhang, X. Fan, Utilization of MoS₂ nanosheets to enhance the photocatalytic activity of ZnO for the aerobic oxidation of benzyl halides under visible light, *Ind. Eng. Chem. Res.* 55 (32) (2016) 8726–8732.
- [8] A. Ghorai, S. Bayan, N. Gogurla, A. Midya, S.K. Ray, Highly luminescent WS₂ quantum dots/ZnO heterojunctions for light emitting devices, *ACS Appl. Mater. Interfaces* 9 (2017) 558–565.
- [9] Y. Wang, A. Hu, Carbon quantum dots: synthesis, properties and applications, *J. Mater. Chem. C* 2 (2014) 6921.
- [10] Z. Zhang, T. Zheng, X. Li, J. Xu, H. Zeng, Progress of carbon quantum dots in photocatalysis applications, *Part. Part. Syst. Charact.* 33 (2016) 457–472.
- [11] T. Sh Atabaev, Doped carbon dots for sensing and bioimaging applications: a minireview, *Nanomaterials* 8 (2018) 342.
- [12] M. Han, S. Zhu, S. Lu, Y. Song, T. Feng, S. Tao, J. Liu, B. Yang, Recent progress on the photocatalysis of carbon dots: Classification, mechanism and applications, *Nanotoday* 19 (2018) 201–218.
- [13] P. Atkin, T. Daeneke, Y. Wang, B.J. Carey, K.J. Berean, R.M. Clark, J.Z. Ou, A. Trinchì, I.S. Cole, K. Kalantar-zadeh, 2D WS₂/carbon dot hybrids with enhanced photocatalytic activity, *J. Mater. Chem. A* 4 (2016) 13563.
- [14] S. Sahu, B. Behera, T.K. Maiti, S. Mohapatra, Simple one-step synthesis of highly luminescent carbon dots from orange juice: application as excellent bio-imaging agents, *Chem. Commun.* 48 (2012) 8835–8837.
- [15] S. Srivastava, R. Sinha, D. Roy, Toxicological effects of malachite green, *Aquat. Toxicol.* 66 (2004) 319–329.
- [16] G. Parshetti, S. Kalme, G. Saratale, S. Govindwar, Biodegradation of malachite green by *Kocuria rosea* MTCC 1532, *Acta Chim. Slov.* 53 (2006) 492–498.
- [17] W. Zhang, X. Xiao, L. Zheng, C. Wan, Fabrication of TiO₂/MoS₂@zeolite photocatalyst and its photocatalytic activity for degradation of methyl orange under visible light, *Appl. Surf. Sci.* 358 (2015) 468–478.
- [18] S. Cao, T. Liu, S. Hussain, W. Zeng, X. Peng, F. Pan, Hydrothermal synthesis of variety low dimensional WS₂ nanostructures, *Mater. Lett.* 129 (2014) 205–208.
- [19] N. Huo, Z. Wei, X. Meng, J. Kang, F. Wu, S.-S. Li, S.-H. Wei, J. Li, Interlayer coupling and optoelectronic properties of ultrathin two-dimensional heterostructures based on graphene, MoS₂ and WS₂, *J. Mater. Chem. C* 3 (2015) 5467.
- [20] H. Ding, L.-W. Cheng, Y.-Y. Ma, J.-L. Kong, H.-M. Xiong, Luminescent carbon quantum dots and their application in cell imaging, *New J. Chem.* 37 (2013) 2515–2520.
- [21] S. Zhou, J. Chen, L. Gan, Q. Zhang, Z. Zheng, H. Li, T. Zhai, Scalable production of self-supported WS₂/CNFs by electrospinning as the anode for high-performance lithium-ion batteries, *Sci. Bull.* 61 (3) (2016) 227–235.
- [22] S.M. Notley, High yield production of photoluminescent tungsten disulphide nanoparticles, *J. Coll. Interf. Sci.* 396 (2013) 160–164.
- [23] M. Zhou, Z. Zhang, K. Huang, Z. Shi, R. Xie, W. Yanga, Colloidal preparation and electrocatalytic hydrogen production of MoS₂ and WS₂ nanosheets with controllable lateral sizes and layer numbers, *Nanoscale* 8 (2016) 15262.
- [24] Y. Yang, J. Cui, M. Zheng, C. Hu, S. Tan, Y. Xiao, Q. Yang, Y. Liu, One-step synthesis of amino-functionalized fluorescent carbon nanoparticles by hydrothermal carbonization of chitosan, *Chem. Commun.* 48 (2012) 380–382.
- [25] H. Li, X. He, Z. Kang, H. Huang, Y. Liu, J. Liu, S. Lian, C.H.A. Tsang, X. Yang, S.-T. Lee, Water-soluble fluorescent carbon quantum dots and photocatalyst design, *Angew. Chem.* 49 (2010) 4430–4434.
- [26] Z. Gan, H. Xu, Y. Hao, Mechanism for excitation-dependent photoluminescence from graphene quantum dots and other graphene oxide derivatives: consensus, debates and challenges, *Nanoscale* 8 (2016) 7794.
- [27] J. Lee, K. Kim, W.I. Park, B.H. Kim, J.H. Park, T.H. Kim, S. Bong, C.H. Kim, G.S. Chae, M. June, Y. Hwang, Y.S. Jung, S. Jeon, Uniform graphene quantum dots patterned from self-assembled silica nanodots, *Nano Lett.* 12 (2012) 6078.
- [28] Q.F. Xu, Q. Zhou, Z. Hua, Q. Xue, C.F. Zhang, X.Y. Yang, D.Y. Pan, M. Xiao, Single-particle spectroscopic measurements of fluorescent graphene quantum dots, *ACS Nano* 7 (2013) 10654.
- [29] J. Sun, S.W. Yang, Z.Y. Wang, H. Shen, T. Xu, L.T. Sun, H. Li, W.W. Chen, X.Y. Jiang, G.Q. Ding, Z.H. Kang, X.M. Xie, M.H. Jiang, Ultra-high quantum yield of graphene quantum dots: aromatic-nitrogen doping and photoluminescence mechanism, *Part. Part. Syst. Charact.* 32 (2015) 434.
- [30] S.J. Hazarika, D. Mohanta, Exfoliated WS₂ nano-sheets: Optical, photocatalytic and nitrogen adsorption/desorption characteristics, *Bull. Mater. Sci.* 41 (6) (2018) (In Press).
- [31] S.J. Hazarika, D. Mohanta, Inorganic fullerene-type WS₂ nanoparticles: processing, characterization and its photocatalytic performance on malachite green, *Appl. Phys. A* 123 (2017) 381.

- [32] K. Yang, B. Chen, L. Zhu, Graphene-coated materials using silica particles as a framework for highly efficient removal of aromatic pollutants in water, *Sci. Rep.* 5 (2015) 11641.
- [33] G.K. Ramesha, A. Vijaya Kumara, H.B. Muralidhara, S. Sampath, Graphene and graphene oxide as effective adsorbents toward anionic and cationic dyes, *J. Coll. Interf. Sci.* 361 (2011) 270–277.
- [34] U.I. Gaya, A.H. Abdullah, Heterogeneous photocatalytic degradation of organic contaminants over titanium dioxide: a review of fundamentals, progress and problems, *J. Photochem. Photobiol. C* 9 (2008) 1–12.